Curriculum Vitae

The author was born in Cleveland, Ohio on September 30, 1965. He attended the University of Rochester from 1983 to 1987, and graduated Magna Cum Laude with Distinction with a Bachelor of Science degree in 1987. He continued at the University of Rochester in 1987 and began studies in Physics. He pursued his research in Particle Physics under the direction of Professor Thomas Ferbel and received the Master of Arts degree in 1989.

ACKNOWLEDGMENTS

The work involved in this thesis necessarily involved a collaboration with many individuals. The construction and operation of a large experiment such as D-Zero can only be possible after years and countless hours of effort by hundreds of dedicated researchers working from many sides toward a common and sometimes quite distant goal. In particular I would like to thank all of the people who kept the Test Beam working day and night during the 1990 and 1991 runs. Many thanks go to my advisor Tom Ferbel for his good cheer and tireless editorial guidance during the preparation of this thesis and also to Jerry Blazey for all of his help over the past seven years. I want to send my warmest wishes to all of my officemates and friends who have always been a joy to work with. And I would especially like to thank my parents for their continued support and encouragement through the full quarter century of my formal education. Finally, I would like to gratefully acknowledge the United States Department of Energy for their support of the research presented here.

ABSTRACT

Fermi National Accelerator Lab (Fermilab) is the site of the world's highest energy particle accelerator. The D-Zero experiment is one of two at Fermilab studying proton-antiproton collisions at center of mass energies of 1.8 TeV. An analysis of the response of the D-Zero central calorimeter to single electrons and pions has been performed under a variety of operating conditions. The data were acquired from the Load-2 D-Zero Test Beam run, in which beam tests of calorimeter modules were performed between July 1991 and January 1992.

The response of modules from the D-Zero central calorimeter was obtained for single electrons and pions in the energy range of 2 through 150 GeV, and implications of these measurements were explored for the energy response to hadronic jets in the calorimeter.

The effects of added oxygen, tetramethylgermanium (TMG), and nitrogen for the responses of the calorimeter modules were examined. The additives were found to have similar effects on the signals from electrons and pions. The data with added oxygen were used to calibrate the response of the calorimeter to oxygen concentration in the liquid argon, as measured using the D-Zero liquid argon purity monitoring system.

The response of the calorimeter to electrons and pions was also studied for varying charge collection fields. An analysis of the data suggests that the signal (ionization) in typical pion showers contains a greater amount of dense ionization than for the case of electron showers. However, the difference was not found to be sufficiently large enough to allow improvement of compensation in the calorimeter by the addition of photosensitive dopants or by operating at higher charge collection fields.

Contents

List of Tables viii

List of Figures x

1 Introduction 1

1.1 The Standard Model of High Energy Physics 3

1.2 Physics Signals at High Energy Colliders 6

1.2.1 Jet Production and Perturbative QCD 6

1.2.2 Jets in Electroweak Processes 9

2 Calorimetry in High Energy Physics and the D-Zero Detector 11

2.1 The D-Zero Detector 11

2.1.1 Central Tracking 12

2.1.2 D-Zero Calorimetry 14

2.1.3 Muon Detection 15

2.2 Principles of Calorimetry 15

2.2.1 Electromagnetic Showers 16

2.2.2 Energy Resolution for Electromagnetic Showers 20

2.2.3 Hadronic Showers 21

2.2.4 Energy Resolution for Hadronic Showers 22

2.2.5 Compensation 23

2.3 Structure of the D-Zero Calorimeters 25

3 The D-Zero Test Beam **28**

3.1 Configuration at the 1991 Test Beam 29

3.1.1 CC Modules 29

3.1.2 The Test-Beam Transporter 29

3.2 The NW beamline 32

3.2.1 The High-Energy Configuration 32

3.2.2 Low-Energy Configuration 34

4 Energy Response of the D-Zero Central Calorimeter **36**

4.1 Systematics 36

4.1.1 Cherenkov Leaks and Pressure Offsets 37

4.1.2 Momentum Distributions and Muon Contamination 38

4.1.3 Momentum Offsets 41

4.1.4 Corrections to the Low Energy Data 43

4.2 Data Selection and Energy Response 44

4.2.1 Selections Applied to All Data 45

4.2.2 Additional Criteria for Low Energies 46

4.2.3 Criteria for High Energies 46

4.2.4 Linearity of Calorimeter Response 47

4.3 Energy Resolution of the Calorimeter 50

4.4 Longitudinal Leakage at High Energy 50

5 Correction of the Energy-Scale for Jets Using Data from the Test Beam **55**

5.1 Introduction – Effect of Response to Low-Energy Particles 55

5.2 Other Systematics 56

5.3 Application of Data from the Test Beam 57

5.4 Extraction of Corrected Response to Jets 60

6 Studies of Effects of Additives and Corrections to Calorimeter Response **62**

6.1 Response of D-Zero Argon Purity Monitors to Additives 64

6.2 Response of the Calorimeter to Additives 70

6.3 Resolution of the Calorimeter with Additives 71

6.4 Corrections to the Responses of the Calorimeters Using β Cells . . . 73

6.5 Correcting response Using α Cells 76

6.6 Summary 78

7 High Voltage Dependence of Calorimeter Response and Ionization Content of Particle Showers **79**

7.1 High Voltage Response with Clean Argon and with Added Oxygen . 80

7.2 High Voltage Dependence of $\frac{e}{\pi}$ Response 86

7.3 Summary of High Voltage Scan Data 88

8 Conclusions **94**

8.1 Low-Energy Response of the Calorimeter and the Jet Energy Scale 94

8.2 Response Corrections 95

8.3 Calorimeter High Voltage Scans and Characteristics of Ionization for Electron and Pion Showers 95

Bibliography **97**

A The D-Zero Liquid Argon Purity Monitors **102**

A.1 Sensors 103

A.2 Data Acquisition 107

List of Tables

1.1 Particles of The Standard Model 5

4.1 Thresholds for Cherenkov Radiation for Pions 42

4.2 Corrections to the observed pion signals at low energy 44

4.3 Reconstructed Energies (without small corrections for muon contamination) 49

4.4 Parametrization of events with leakage to a sum of three gaussian functions of the form: Const $\times$ exp$[(\mathrm{E} - \mathrm{Mean})^2/2\sigma^2]$. 54

6.1 Additives to liquid argon during 1991 test beam run 63

6.2 Signals observed in test cells after consecutive mixing in of additives to the argon 69

6.3 Response of the calorimeter to electrons and pions as a function of additives in the liquid argon 71

6.4 Resolution as a function of additives 72

6.5 β cell response ratios for test beam oxygen studies and estimated oxygen concentrations (ppm) 75

6.6 Response of D-Zero calorimeters relative to 1991 test beam. 76

7.1 Fitted shower components for electron and pion responses in clean argon. 83

7.2 Fitted shower components for electron and pion responses after addition of oxygen. 85

7.3 Calorimeter high voltage response for clean argon – 10 GeV 88

7.4 Calorimeter high voltage response after first oxygen addition – 10 GeV 88

7.5 Calorimeter high voltage response after second oxygen and 4 ppm nitrogen addition – 10 GeV 89

7.6 Calorimeter high voltage response after TMG addition – 10 GeV . . 89

7.7 Calorimeter high voltage response after 100 ppm nitrogen addition – 10 GeV 90

7.8 Calorimeter high voltage response for clean argon – 100 GeV 90

7.9 Calorimeter high voltage response after first oxygen addition – 100 GeV 91

7.10 Calorimeter high voltage response after second oxygen and 4 ppm nitrogen addition – 100 GeV 91

7.11 Calorimeter high voltage response after TMG addition – 100 GeV . 92

7.12 Calorimeter high voltage response after 100 ppm nitrogen addition – 100 GeV 92

7.13 Calorimeter high voltage response for clean argon – 5 GeV 93

List of Figures

1.1 Typical graphs contributing to 2-jet and 3-jet production. 9

2.1 The D-Zero Detector 13

2.2 Cross sections for energy loss mechanisms for electromagnetic processes 19

2.3 Energy deposition as a function of depth for a 10 GeV electron shower 20

2.4 Typical Unit Cell in The D-Zero Calorimeter 25

2.5 Cutaway View of the D-Zero Calorimeters 27

3.1 Cross section of the D-Zero central calorimeter 30

3.2 Test Beam Cryostat Transporter System 31

3.3 High Energy Beamline 33

3.4 Low Energy Beamline 35

4.1 Arrangement of scintillator tags downstream of the calorimeter for the detection of energy leakage. 37

4.2 Momentum distributions for 2 GeV/c and 5 GeV/c particles. 39

4.3 Fits to pion and muon momentum distributions. 41

4.4 Hall probe reading versus magnet readback current. 43

4.5 Calorimeter response to pions and electrons for 2 through 150 GeV/c 48

4.6 Fits to the energy resolution for electrons and pions of momentum between 2 and 150 GeV/c 51

4.7 Leakage effects for high energy pion shower 52

4.8 Pion response at 150 GeV/c 53

5.1 The systematic uncertainty in measurement of jet energy for the CDF experiment. 57

5.2 Inclusive E_t Spectrum From CDF 58

5.3 Energy response of D-Zero central calorimeter to electrons and pions relative to the response at 150 GeV. 60

5.4 Estimated response of the D-Zero central calorimeter for jets in the energy range of 20-200 GeV 61

6.1 History of the signal observed in an α cell 66

6.2 Response of a β cell to additives 67

6.3 Normalized electron response versus energy after the addition of the first sample of oxygen 70

6.4 The ratio of the response at 0.9 kV/cm to that at 10.9 kV/cm, for a β-type test cell as a function of oxygen contamination 74

7.1 α and β ionization cell responses as a function of charge collection electric field. 81

7.2 Fits to 100 GeV/c pion response with and without a heavily ionizing component. 83

7.3 Voltage dependence of response for 100 GeV electrons and pions. . . 84

7.4 The $\frac{e}{\pi}$ response as a function of electric field for 10 and 100 GeV. . 87

A.1 α and β sensor configurations 103

A.2 α spectrum and response versus field for different oxygen contaminations 104
A.3 β spectrum and response versus field for different oxygen contaminations 106
A.4 System Block Diagram 107
A.5 Ground/Shield Configuration for Test Cells 109

FOREWORD

The D-Zero experiment is a large collaborative effort. Thirty-six institutions and nearly 400 physicists and students are participating in the experiment at present. The University of Rochester group has been active in several facets of the construction and operation of the experiment. These include being responsible for the design, construction, and installation of liquid argon purity and temperature monitoring systems, making significant contributions to the 1987, 1990, and 1991 beam tests at Fermilab, being deeply involved in the analysis projects undertaken by D-Zero's quantum chromodynamics (QCD) and top physics groups, and participation in research and development projects in scintillating fiber tracking technology for the D-Zero upgrade.

I have been involved in a variety of projects throughout my participation in the D-Zero experiment. I designed and supervised construction of the front end electronics for the D-Zero argon purity monitoring system, aided in the design and construction of calibration pulser boards for those electronics, and worked on the installation and optimization of these systems throughout the D-Zero cryostats, as well as the necessary control and analysis software. I have also worked on detailed simulations of the purity monitor systems. I worked on the optimization of the low energy tertiary beamline configuration at the D-Zero Test Beam and was responsible for optimizations, upgrades, and changes to the fast beam-trigger electronics for the 1991 D-Zero Test Beam run and assumed an active role in the day to day operations and data taking during the 1990 and 1991 test-beam runs.

My analysis projects have included an analysis of the response of the the D-Zero calorimeter to low energy electrons and hadrons, the effects of various additives to the liquid argon on the response for electrons and pions, and the effect of high voltage field adjustment on the response.

Chapter 1

Introduction

The direction of modern elementary particle physics was, in some sense, set in the period 1910-1930 with the increase in exploration of atomic and subatomic phenomena. The purpose of particle physics is to uncover the basic constituents of matter and the forces by which they interact. Prior to the 1900s all natural phenomena were presumed to have their origin in only two basic forces, electromagnetism and gravitation. As properties of the nucleus were explored, it soon became apparent that two new forces had to be added to the list to describe two new phenomena: the binding of nucleons and β decay. The discovery of scores of unexpected subatomic particles in the 1960s brought into question their elementary nature, and commenced the search for a more basic understanding of the structure of matter.

The prototype for a particle physics experiment can be found in Rutherford's discovery of the nucleus in 1911. Rutherford was able to infer the existence of a massive point-like core in gold atoms by observing the distribution of α particles scattered from a thin gold foil. The finest structure observable in scattering experiments is determined by the size or wavelength of the particle used as a probe. With

the construction of the first particle accelerators, the Van DeGraaf generator and the cyclotron in the early 1930s, the availability of higher energy particles made it possible to probe deeper into the nucleus and uncover the previously unseen structure within it. Modern accelerators are capable of probing much deeper into matter and of providing the colliding particles with enough energy to create many of the massive fundamental particles that are expected on the basis of present theories.

The Fermi National Accelerator Laboratory (Fermilab) is the site of the world's highest energy accelerator, the Tevatron, a machine housed in a ring that is four miles in circumference, and is capable of accelerating protons to energies of 900 GeV. By producing anti-protons and accelerating them oppositely around the ring, center of mass energies of 1.8 TeV are reached in $p\bar{p}$ collisions.

Fermilab also supports an active program of fixed target experiments, where the primary proton beam from the Tevatron is transported along beam lines and collided directly with targets at experimental sites, or the proton beam is used to produce secondary beams of hadrons, leptons, or photons, which are then transported to the site of a fixed target experiment.

This dissertation presents measurements of the performance of detector modules used in the D-Zero experiment at Fermilab. Results of beam tests performed on Central Calorimeter (CC) modules from D-Zero will be the focus of subsequent chapters. The data to be presented were acquired at the D-Zero Test Beam site in Building A of the Neutrino-West Beamline at Fermilab between July 1991 and January 1992. Chapter 2 contains a description of the D-Zero detector and a review of the principles of sampling calorimeter detectors. The D-Zero Test Beam experiment is described in chapter 3. The response of the calorimeter modules to electron and pion beams in the momentum range of 2-150 GeV/c are presented in chapter 4, and the implications of the observed response to single particles on

the expected response to hadronic jets in Chapter 5. The effects of adding oxygen and and other materials to the calorimeter modules will be discussed in chapter 6. And chapter 7 will deal with the dependence of the response of the calorimeter on the imposed electric field across the module gaps. The goals of these subsequent chapters will be to provide information useful for understanding the response of the D-Zero detector to hadronic jets, to provide a method to calibrate the responses of the various D-Zero calorimeters based on argon quality, and to find evidence of any differences in the character of ionization present in electromagnetic and hadronic particle showers. In the remainder of this chapter we will develop several of the ideas that motivated the D-Zero experiment.

1.1 The Standard Model of High Energy Physics

The Standard Model of particle physics has been particularly successful at describing all known phenomena at energy scales from fractions of an electron volt (eV) to over 100 GeV (10^{11} eV) [1, 2]. Combined with the theory of gravitation, it seeks to explain the nature of all physical processes. The Standard Model includes the electro-weak theory of Glashow, Weinberg, and Salam, which offers a unified model of the weak and electromagnetic forces, and quantum-chromodynamics (QCD) the theory of strong interactions of the constituents of hadrons. In the Standard Model, three types of fundamental particles, namely quarks and leptons (the fermions), and gauge bosons, constitute all the forms of matter.

Quarks are grouped into left-handed (L) helicity doublets of weak isospin and associated with each quark doublet is another left-handed lepton doublet. Each pair of these fermion doublets is referred to as a generation. The right-handed (R) fermions appear as singlets in weak isospin that do not participate in weak interactions which couple members of the doublets. Right-handed neutrinos are assumed not to exist in nature. The Standard Model does not constrain the number of these generations, but so far there is only experimental evidence for three of them. Each of the six types or "flavors" of quarks possesses an additional internal degree of freedom called "color", which, without violating the Pauli exclusion principle, allows any two quarks to occupy the same energy state within hadronic matter. Color corresponds to the charge or source of the strong force, and only quarks and gluons, and particles composed of them, participate in strong interactions.

In the Standard Model, the gauge bosons mediate the forces between the fermions. Charged particles are the sources of photons, and photons can be exchanged in electromagnetic interactions of such particles. Colored particles (the quarks and gluons) participate in strong interactions through the exchange of gluons. The weak force is transmitted through the exchange of W and Z bosons (intermediate vector bosons (IVBs)), which couple primarily to particles within the same weak isospin doublet. Table 1.1 summarizes the properties of the fundamental particles in the Standard Model. In gauge theories, the gauge bosons are massless. The W and Z masses arise from a process known as spontaneous symmetry breaking that is related to the presence of a massive scalar boson called the Higgs.

A theory is judged by its predictive as well as its descriptive successes. Currently, the Standard Model contains many free parameters (such as the quark and lepton masses, strong coupling constant(α_S), etc.) whose values cannot be calculated from the theory. Three charged leptons (e,μ,τ) and two of their neutral

Table 1.1: Particles of The Standard Model

Fundamental Fermions					
Quarks				Color Charge	Electric Charge
SU(2) Doublet	$\begin{pmatrix} u_L \\ d_L \end{pmatrix}$	$\begin{pmatrix} c_L \\ s_L \end{pmatrix}$	$\begin{pmatrix} t_L \\ b_L \end{pmatrix}$	r,g,b	$+\frac{2}{3}$ $-\frac{1}{3}$
SU(2) Singlets	u_R d_R	c_R s_R	t_R b_R	r,g,b	$+\frac{2}{3}$ $-\frac{1}{3}$
Leptons					
SU(2) Doublet	$\begin{pmatrix} (\nu_e)_L \\ e_L \end{pmatrix}$	$\begin{pmatrix} (\nu_\mu)_L \\ \mu_L \end{pmatrix}$	$\begin{pmatrix} (\nu_\tau)_L \\ \tau_L \end{pmatrix}$		0 -1
SU(2) Singlet	e_R	μ_R	τ_R		-1
	Bosons		Mass (GeV/c^2)		
γ		photon	0		0
$W^\pm$		IVB	80.22 ± 0.26		± 1
Z^0		IVB	91.173 ± 0.020		0
g		Gluon	0	$r\bar{b}, r\bar{g}, b\bar{g}, b\bar{r}, g\bar{r}, g\bar{b}, \frac{(r\bar{r}-b\bar{b})}{\sqrt{2}}, \frac{(r\bar{r}+b\bar{b}-g\bar{g})}{\sqrt{6}}$	0
H		Higgs	> 42		0

partners (ν_e and ν_μ) have been observed. Direct evidence exists for five of the six quarks (u,d,c,s,and,b), and for the $W^\pm$, Z^0 and the gluon bosons. The observation of the sixth quark (top or t) and third neutrino (ν_τ) are essential to the confirmation of the Standard Model. Also, present experiments have provided no evidence for the existence of the Higgs boson. Thus, although this theory describes beautifully the interactions of all known particles, it is clearly far from complete [3].

1.2 Physics Signals at High Energy Colliders

Physics signals used to test predictions of the Standard Model and to measure free parameters must be extracted from a background of less interesting events. The transverse momentum (p_T) is often the most important kinematic variable in studying $p\bar{p}$ collisions. Where p_T is the momentum component of collision products in the direction transverse to the beam axis.

Production at high-p_T is often of primary interest, because such events correspond (via the Uncertainty Principle) to interactions at small distances. Events at small angles to the beam are often dominated by leftover debris from scattering hadrons in collisions that do not directly involve the constituents. Many important physics signatures involve non-interacting particles (such as neutrinos), whose presence can be inferred from the transverse momentum that they carry away in an event (this is usually termed missing transverse momentum or $\not{p}_T$). Since the p_T of the colliding beams is essentially zero, a sum over the p_T values of all particles produced in a collision should, within the experimental resolution, be consistent with zero. The total momentum sum is not used to infer the presence of non-interacting particles, because much of an event's final-state momentum (carried by spectator quarks) is lost down the beamline and escapes undetected.

Events within potentially interesting physics often contain one or more of the following signatures: high-p_T charged leptons, photons, jets of hadrons and large-$\not{p}_T$. We give examples of several such underlying processes in the discussion below.

1.2.1 Jet Production and Perturbative QCD

The realization that hadrons consist of a bound collection of point-like partons has been one of the major advances in high energy physics in the last 30 years. These partons are now equated with the quarks and gluons of QCD. The parton

structure of hadrons was experimentally inferred from deep inelastic scattering of neutrinos and electrons from protons. However, an isolated parton has never been observed outside of a parent hadron.

The scattering and liberation of a parton that contains a large fraction of the parent hadron's momentum can be recognized through the emission of a well collimated spray of particles at a large angle relative to the beamaxis. This spray or "jet" of hadrons arises from the hadronization process (constituents fragmenting into physical particles) that takes place at distances that are large compared to the size of the parent hadron. These jets follow the directions of the scattered partons, and have approximately the same momentum and energy as their parent constituents.

A reliable description of scattering at large p_T is available within the framework of perturbative QCD. This is because high-p_T jets signal the presence of large four-momentum transfers (q^2) between partons. At large q^2 quarks and gluons couple weakly (small α_S) and perturbative QCD can therefore be used to calculate yields. This weak coupling at large q^2 has its origin in the fact that gluons interact with quarks as well as with each other. This is different than for the case of quantum electrodynamics (QED), where the analogous photons carry no electronic charge and therefore have no self interaction. These additional gluon interactions lead to a strong coupling constant that decreases with increasing q^2 of the mediating gluon. At low q^2 exchanges of gluons between gluons and quarks provides the tight binding of quarks and gluons into colorless hadron states. Thus, to predict results of strong interactions between quarks and gluons at low q^2 requires a full theory of binding that is not currently available. However, in high q^2 collisions, the partons have small couplings, and their interactions can therefore be calculated through a perturbative expansion. Thus, the larger the q^2 in a scattering process, the closer do the partons appear to behave as free non-interacting states.

There are several models of hadronization (or fragmentation) for scattered partons. One particularly intuitive scheme is based on a string fragmentation method. Here, the partons are described as connected by strings which can break and form quark-antiquark pairs. As valence quarks in a hadron begin to separate after a collision, the potential energy contained in the collimated color field grows almost linearly with separation. Eventually, it becomes energetically feasible for quark-antiquark pairs to be created. These pairs can form colorless mesons which may separate again, producing other meson pairs, etc. All these particles follow the initial momentum direction of the constituent, and form the emitted hadronic jet.

Jets are composed from a variety of particles with different energies that can be detected either through their strong or electromagnetic interactions in matter. To measure the properties of jets it is necessary to have a detector with good energy linearity and resolution for particles whose signals (deposited energy) may vary over a wide dynamic range and correspond to rather different physical processes.

The analysis of jet events is important for studying a wide variety of QCD phenomena. The di-jet invariant mass distribution can reveal the presence of new particle states or production properties of known states. The high center of mass energy at the Tevatron provides ways of studying the q^2 dependence of α_S, i.e., $\alpha_S(q^2)$ at q^2 values higher than ever studied before. For example, $\alpha_S(q^2)$ can be determined directly from the ratio of 2-jet to 3-jet event cross-sections. This is because the 3-jet cross-section is suppressed by a factor of α_S relative to 2-jet production (see Fig. 1.2.1). α_S can also be determined from a comparison of di-jet and direct photon production, where the latter cross-section is proportional in first order to $\alpha_{EM} \cdot \alpha_S$. Any substructure to quarks could manifest itself as a deviation of the inclusive jet cross-section from that expected on the basis of QCD. This is particularly interesting at higher q^2 values beyond current limits on the compositeness scale.

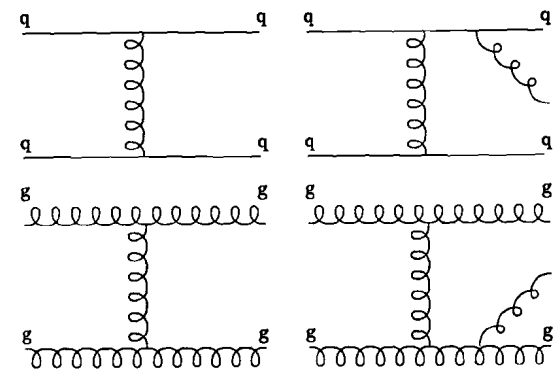

Figure 1.1: Typical graphs contributing to 2-jet and 3-jet production. The cross-sections for 3-jet events (above right) are suppressed by a factor of α_S compared to 2-jet events (above left) due to the extra vertex.

1.2.2 Jets in Electroweak Processes

As an example of the importance of jets in electroweak processes, we focus on the production of top. The discovery of the top quark to complete the last fermion doublet of the Standard Model is one of the most pressing challenges in high energy physics today. Current experimental evidence suggests a top quark of $\geq 91\ \mathrm{GeV/c^2}$ at the 95% confidence level [4]), and suggests that the most accessible channel for the discovery of the top would be the process:

$$\mathrm{gg\ or\ q\bar{q}} \rightarrow \mathrm{t\bar{t}} \rightarrow \mathrm{W^+b} + \mathrm{W^-\bar{b}} \tag{1.1}$$

The favored decay channels (about 5% branching ratio) for observing the top

are where one or both W's decay leptonically:

$$\begin{array}{lllll} gg \text{ or } q\bar{q} \longrightarrow & t\,\bar{t} & \longrightarrow & W^- & \bar{b} \\ & & & \hookrightarrow & \ell^- \; \bar{\nu}_\ell \\ & & \hookrightarrow & W^+ & b \\ & & & \hookrightarrow & \ell^+ \; \nu_\ell \end{array} \tag{1.2}$$

The above process is the "cleanest" decay process for the $t\bar{t}$ pair. Two charged leptons and missing energy will be detected as well as two jets from the b-quark decays. It is relatively easy to measure the properties of single leptons to high precision, however due the low branching ratio for this channel, other processes should be considered for discovery of top. Another interesting channel for finding top is through the $t\bar{t}$ decay into one charged lepton and jets (branching ratio $\approx 30\%$):

$$\begin{array}{lllll} gg \text{ or } q\bar{q} \longrightarrow & t\,\bar{t} & \longrightarrow & W & b \\ & & & \hookrightarrow & \ell \; \nu \\ & & \hookrightarrow & W & b \\ & & & \hookrightarrow & 2 \text{ jets} \end{array} \tag{1.3}$$

Decays in this channel produce one lepton-neutrino pair through one W, two jets from the other W, and two b-jets.

It is necessary for a detector to provide accurate measurements of the properties of jets in order to perform detailed studies of all the above physics issues. The remainder of this thesis is devoted to a study of the calorimetric detectors that provide the basis for such measurements in the D-Zero experiment.

Chapter 2

Calorimetry in High Energy Physics and the D-Zero Detector

As the demands of particle physics have required the study of products of collisions from ever higher energies, the calorimeter has become a preeminent experimental tool. Conceptually, a calorimeter is a detector in which a particle interacts, losing all of its energy, and transferring part of it into a measurable signal. In this chapter we briefly describe the D-Zero detector and present some general features of calorimetric detectors with particular emphasis on those aspects related to the D-Zero calorimeter.

2.1 The D-Zero Detector

The D-Zero detector includes three specialized subdetectors, one for tracking of charged particles near the $p\bar{p}$ interaction point, one for calorimetric energy measurement, and one for detection and momentum measurement of muons. The central tracking detectors are located close to the collision axis. They are surrounded by three hermetic calorimeters that provide nearly 4π coverage. Muons,

which deposit only a small fraction of their energy in the calorimeter, are detected in the D-Zero muon system outside of the calorimeter. Figure 2.1 shows a cutaway view of the entire D-Zero detector. Several references have included extensive descriptions of D-Zero, in particular ref. [5] offers a detailed overview of all the devices and data acquisition systems that comprise D-Zero.

2.1.1 Central Tracking

The D-Zero central detector (CD) is composed of tracking and transition radiation detectors. An inner tracking vertex detector (VTX), is followed by a Transition Radiation Detector (TRD) and an outer drift chamber (the Central Drift Chamber or CDC), all positioned in an axially symmetric fashion about the colliding beams. Also, planar drift chambers are located at small angles on either side of the three forementioned detectors. The inner tracking chamber is used to measure positions of charged tracks before the TRD; these chambers have a spatial precision of 35-80μm; The VTX therefore provides a way for distinguishing an electron candidate from photons converting in the TRD. The TRD contains three concentric sets of polypropylene foils surrounded by a xenon proportional-wire chamber with wires running parallel to the beam. Time of arrival, combined with the total charge collected, and the cluster structure of the charge is used for achieving electron-pion discrimination at a design value of about 50:1 [6]. The outer cylindrical drift chamber, combined with the VTX, provides the production angles of charged particle tracks in any event. The CDC also provides $\frac{dE}{dx}$ measurements of charged particles, which can be used to distinguish unopened e^+e^- pairs (from photon conversions in the TRD) and single electrons. The forward and backward drift chambers consist of sections with radial wires sandwiched between two sections

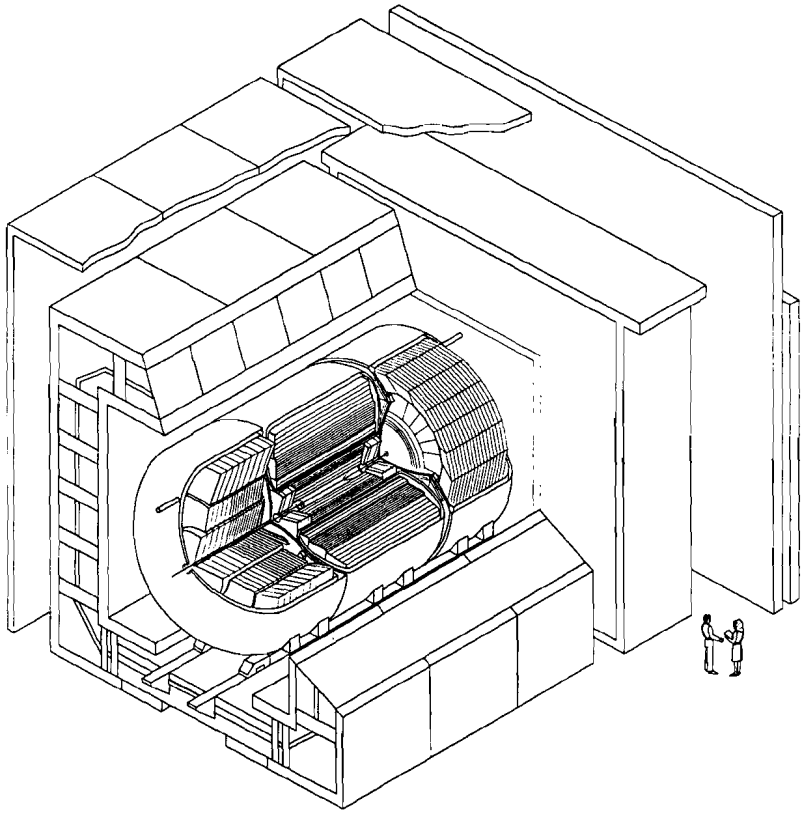

Figure 2.1: The D-Zero Detector

that provide a measure of the pseudorapidity or η[1] coordinate of produced particles. Together, the central and forward/backward drift chambers provide tracking and $\frac{dE}{dx}$ measurements out to $|\eta| \approx 3.5$.

2.1.2 D-Zero Calorimetry

The heart of the D-Zero detector is a uranium/liquid-argon sampling calorimeter used to measure the energies of incident electrons, photons, and hadrons. It is composed primarily of alternating layers of depleted uranium and gaps filled with liquid argon. The calorimeter is divided into three sections, each housed within its own cryostat. The central calorimeter (CC) provides full azimuthal coverage for electromagnetic and hadronic showers for $|\eta| \leq 1$. The two end calorimeters (ECs) extend coverage out to $|\eta| \approx 4$. Each calorimeter is subdivided into electromagnetic, fine hadronic, and coarse (or outer) hadronic sections. Particles incident on the uranium "absorber" layers initiate cascades or "showers" of low energy secondary particles. The interspersed "active" layers of liquid argon are ionized by the charged secondary particles. The ionization charge, which is proportional to the energy of the incident particle, is collected by imposing a high voltage field across the argon layers. Specific details of the construction of the D-Zero calorimeter will be provided in Section 2.3 after a general discussion of the principles of calorimetry in Section 2.2.

[1]The coordinate system at D-Zero is cylindrical, defined by (r, ϕ, η). Where r is the radial distance from the beam axis, ϕ the azimuthal angle, and η is defined as $\eta = -ln\left[tan\left(\frac{\theta}{2}\right)\right]$, where θ is the polar angle relative to the beam axis. The pseudorapidity is used in describing hadronic collisions, because the produced differential charged particle multiplicity depends only weakly on η.

2.1.3 Muon Detection

Muons are identified in D-Zero by their penetration through large amounts of absorber material; their momenta are determined by measuring their deflection in magnetized iron toroids located beyond the calorimeters. The coverage of the muon system extends down to 3° on either side of the beamline. Forward angles are covered by an extension of the initial design to the small angle muon detectors (SAMUS) [7]. Magnetized iron toroids surrounding the calorimeters provide a bending strength equivalent to a transverse momentum impulse of 600 MeV/c. Three sets of multi-layer proportional drift tubes are used for tracking the positions of the muons. There are four layers of wire planes, between the calorimeters and the toroids. Outside the toroids, there are two layers of drift tubes (three planes each) that provide exit directions as well as locations of muons. The total depth of the calorimeters and toroids vary from 18 absorption lengths at small polar angles to 13 absorption lengths at $\eta = 0$. This amount of material stops essentially all hadrons, and provides identification of muons within cores of jets of hadrons.

2.2 Principles of Calorimetry

Calorimeters are well suited to the demands of D-Zero and other modern experiments that study particle collisions at high center of mass energies. In particular, calorimeters provide a technically viable means for measuring energies of high-energy hadrons, leptons, and photons, and for inferring any missing momentum, with sufficient resolution and triggering capability, at an acceptable cost. Among the advantages of calorimeters are [9]:

- The dimensions of calorimeters necessary for full energy containment scale only logarithmically with energy of the incident particle.

- Because calorimetric measurements are based on statistical sampling of a particle's energy, the relative precision of measurement increases with incident particle energy.
- Calorimeters are sensitive to both charged and neutral particles.
- Calorimeters do not require a magnetic field for energy measurement.
- Calorimeters can be used to distinguish hadrons from photons and electrons through differences in patterns of energy deposition.
- Finely segmented detectors can provide precise measurements of positions and angles of incident particles.

When traversing matter, a particle will generally interact, losing part of its energy and exciting the medium in the process. The specific interaction depends on the energy and the nature of the particle, and can involve electromagnetic, strong, or more rarely, weak interactions between the particle and the constituents of the medium. The following sections describe methods by which leptons, photons, and hadrons may interact and be absorbed within a calorimeter.

2.2.1 Electromagnetic Showers

Various mechanisms contribute to a particle's energy loss and eventual absorbtion in a calorimeter. Electromagnetic (EM) interactions of charged particles with matter are the best understood energy-loss mechanisms. Photon (γ) and electron showers are very similar except, essentially, for the first interaction. Photons lose their energy primarily through pair production, Compton scattering, and the photoelectric effect. Electrons and positrons lose energy principally via bremsstrahlung and ionization. The relative importance of all these processes depends strongly on the particle energy and the atomic number (Z) of the medium.

For energies of more that several MeV, the absorption of photons and electrons is a multi-step process in which particle multiplication (shower development) occurs within the calorimeter. For example, a high energy photon ($\gtrsim 1$ GeV) incident on the calorimeter will produce an e^+e^- pair after traversing a certain amount of material (typically $\approx \frac{9}{7}$ of a radiation length). The electron and positron will radiate other photons (bremsstrahlung), until they lose sufficient energy so that the cross section for ionization of the medium becomes comparable to that for bremsstrahlung (critical energy ϵ_c). If the bremsstrahlung γs have sufficient energy, they will also produce e^+e^- pairs. An electromagnetic shower develops in the calorimeter in this manner until the mean energies of the secondary particles reach the critical energy, the point at which particle multiplication effectively ceases. For energies above ϵ_c, photons interact by producing pairs and electrons predominantly lose their energy by creating new photons. Below ϵ_c, electrons lose more energy by ionizing the medium than by bremsstrahlung and below $\approx \frac{1}{3}\epsilon_c$ photons interact primarily through Compton scattering or the photoelectric effect. Thus, a high energy incident γ or electron will initiate a shower of thousands of different particles, γs, electrons, positrons, the majority of which will eventually degrade to very soft (low energy) particles. It has been shown in Monte Carlo calculations, that for 10 GeV electrons showering in lead or uranium, approximately 40% of the detectable energy is deposited by particles of energy below 1 MeV [8]

All of the energy-loss mechanisms by electrons and photons are well understood on the basis of quantum electrodynamics (QED). Figure 2.2 shows calculations of the cross sections for the individual processes, as a function of incident energy, in materials with three different Z values: carbon (Z=6), iron (Z=26), uranium (Z=92) [10, 11]. At high energies, radiative energy losses dominate in all materials, however the specific energy at which Compton scattering dominates pair production, or ionization loss dominates bremsstrahlung, strongly depends on the

material and scales roughly with the inverse of atomic number Z.

Since the processes that control EM shower development depend on the electron density of a material, it is possible to some extent to describe many features of EM showers in a material independent way. The radiation length (X_0) is defined as the depth after which high energy electrons traversing a material lose on average 63.2% (1.e., $1-\frac{1}{e}$) of their initial energy to bremsstrahlung. A high energy photon travels on average a distance of $\frac{9}{7}X_0$ before converting to an e^+e^- pair. The radiation length is given approximately by:

$$X_0 \approx \frac{180A}{Z^2}\left(in\frac{g}{cm^2}\right) \tag{2.1}$$

where A is the nucleon number of the medium. The critical energy at which electrons lose equal amounts of energy to bremsstrahlung and ionization is given approximately by:

$$\epsilon_c \approx \frac{550}{Z}(\mathrm{MeV}) \tag{2.2}$$

The development of EM showers is nearly material independent when expressed in terms of X_0. Figure 2.3 shows the longitudinal profile of a 10 GeV electron shower in Al, Fe, and Pb as obtained with an EGS4 simulation [9]. The shower profile essentially scales with X_0, and the differences can be understood in light of the differences in cross sections shown in Fig. 2.2. Because electron radiation and particle multiplication continue down to lower energies, remnants of the shower do not get absorbed as easily, the shower maximum is therefore deeper for higher-Z materials.

Muons also lose energy through electromagnetic interactions with matter. However, QED processes such as bremsstrahlung are suppressed by a factor of $\left(\frac{m_\mu}{m_e}\right)^2$. Typically, the critical energy for muons is greater than 200 GeV. Most muons produced in $p\bar{p}$ collisions at D-Zero will therefore lose energy in a calorimeter primarily

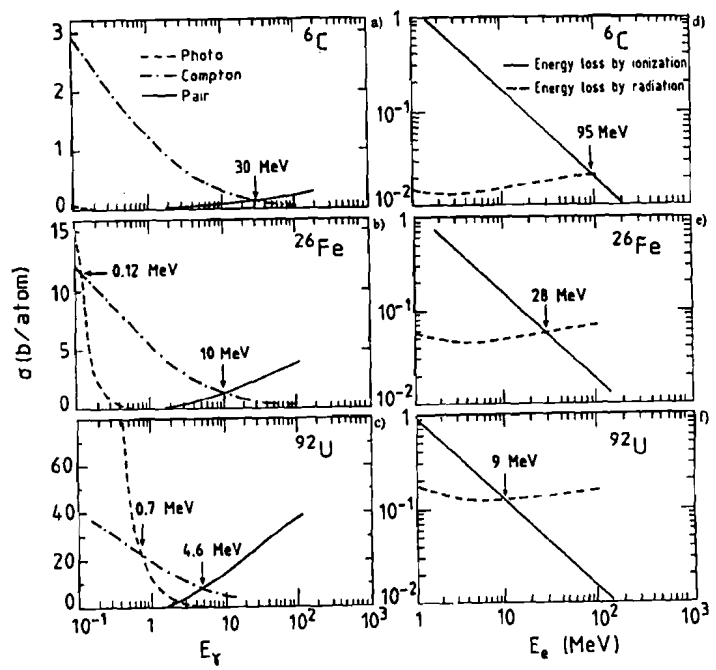

Figure 2.2: Energy loss mechanisms for electromagnetic processes as a function of energy. Photon cross sections for pair production, Compton scattering, and the photoelectric effect in carbon (a), iron (b), and uranium (c). The fraction of total energy deposited by electrons through ionization and radiation in carbon (d), iron (e), and uranium (f) [10, 11].

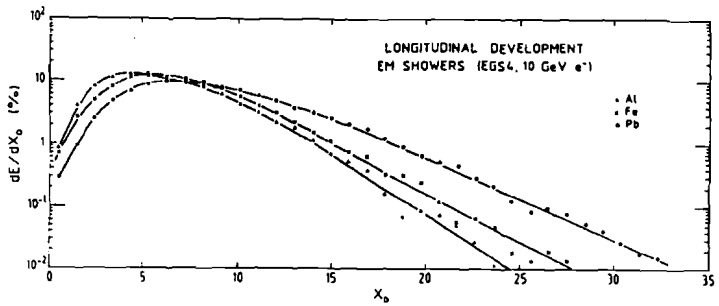

Figure 2.3: Energy deposition as a function of depth (in radiation lengths) for a 10 GeV electron shower in aluminum, iron and lead. Results from EGS4 calculations [13].

through ionization. The energy loss per unit length for these processes is given by the Bethe-Bloch formula [12]. Highly relativistic muons deposit typically 2-3 MeV of energy per radiation length [9], and can therefore be absorbed only by very substantial amounts of matter.

2.2.2 Energy Resolution for Electromagnetic Showers

The measured signal in a calorimeter is derived from the ionization electrons produced in a shower. The total number of ionization electrons produced (n) is proportional to the incident energy (E), and is governed by statistical processes which depend on the nature of the medium. The width or uncertainty (σ) of the observed signal ($S \propto n$) is related to the fluctuations in the detected number of ionization electrons by

$$\sigma(S) \propto \frac{\sqrt{n}}{n} \tag{2.3}$$

If S is proportional to E and to n, we get

$$\sigma(E) \approx \frac{Constant}{\sqrt{E}} \tag{2.4}$$

Only a small fraction of an incident particle's energy is usually measured in a sampling calorimeter. Such devices have high-Z absorber layers alternating with low-Z readout regions. The showers develop primarily in the absorber, and the produced charged-particle tracks ionize the atoms in the active (readout) medium, producing a detectable signal. Using high-Z absorber provides a more compact detector; however, the observed energy resolution is degraded because most of the energy is deposited in the absorber rather than in the active medium. Particles produced in the absorber may never enter the sensitive region of the calorimeter. In particular, electrons liberated in the absorber by low energy photons (e.g., photoelectric effect) will only interact (ionize) with other atoms in the absorber, unless they are produced very close to the surface. The response and resolution of a sampling calorimeter is therefore highly dependent on the choice of active and passive materials and their relative thicknesses.

2.2.3 Hadronic Showers

Although particle production mechanisms governed by the strong interaction are substantially more complicated, the absorption of hadrons within a calorimeter is similar to that of purely electromagnetically-interacting particles. At some point within a calorimeter, a hadron will interact with a nucleus and usually produce mesons (e.g. $\pi^{\pm}, \pi^{0}, K^{\pm}, K^{0}, \eta$). The secondary particles may induce additional reactions further downstream, causing a shower to develop. Also, part of the incident energy will contribute to the breakup of target nuclei. These nuclei will emit a certain number of nucleons and low energy γs, and their remnants will

lose kinetic energy by ionization. In this cascading process some of the produced particles interact only electromagnetically (e.g. $\pi^0 \rightarrow 2\gamma$ or $\eta \rightarrow 2\gamma$ decays). This EM fraction of the hadronic shower (f_{em}) may vary greatly from event to event and the average number of π^0s and ηs produced by incident hadrons will increase slowly with their energy.

Since hadronic shower development is determined largely through nuclear interactions, the shower dimensions are characterized by the mean free path for inelastic nuclear interaction: λ_{int}:

$$\lambda_{int} = 50A^{\frac{1}{3}}\left(\frac{g}{cm^2}\right) \tag{2.5}$$

where the very approximate λ_{int} is the mean free path for collisions of nucleons with nuclei of atomic weight A. (The mean free path for π mesons is greater by 20-50%, depending on A.)

A hadronic shower deposits a large fraction of its energy through interactions of nonrelativistic low-energy recoil protons and neutrons [13]. Since low-energy protons have a specific ionization $< \frac{dE}{dx} >$ which is 10 to 100 times that of minimum ionizing particles (MIPs), the energy detected may be considerably different than for MIPs. The active media in a calorimeter may also suffer from saturation effects caused by the densely ionizing particles. A considerable part of the non-electromagnetic fraction of a hadron shower is due to soft (few MeV) neutrons from nuclear evaporation processes. These neutrons interact through collisions with atomic nuclei, and their contribution to the signal in the calorimeter depends on their energy loss in these collisions.

2.2.4 Energy Resolution for Hadronic Showers

Hadron showers are detected with an energy resolution that is worse than that for EM showers. Because of undetectable shower components, hadrons will, in

general, produce signals smaller than electrons of the same incident energy. Large, non-Gaussian fluctuations in (f_{em}) contribute an additional term to the resolution. And the intrinsic fluctuations in the fraction of energy observed in the sensitive part of the detector can be substantial. Losses to nuclear binding may, for instance, consume up to 40% of the incident energy, with large fluctuations about this percentage [13]. Energy from a hadron shower may also be carried off by neutrinos and muons, escaping total or partial detection in the calorimeter. These intrinsic fluctuations form the ultimate limit for energy resolution of hadrons in a calorimeter. In general the resolution can be written as

$$\sigma_{had}/E = \sqrt{\frac{c_{int}^2 + c_{samp}^2}{E}} + a(E) \tag{2.6}$$

Where a is an additional term contributing to the energy resolution from fluctuations in the electromagnetic fraction of the shower. The latter term vanishes only when a calorimeter's response to the electromagnetic and hadronic components of a shower are the same; a calorimeter with this feature is said to be "compensating".

2.2.5 Compensation

The ratio of the response of a calorimeter to electromagnetic (e) and non-electromagnetic (h) components of hadron showers ($\frac{e}{h}$) is a crucial measure of the performance of a calorimeter for measuring hadron energies. The fluctuations and energy dependence of f_{em} lead to the following effects for hadronic energies measured using a non-compensating ($\frac{e}{h} \neq 1$) calorimeter [9]:

- Monoenergetic hadrons will display a non-Gaussian energy distribution.
- Fluctuations in f_{em} represent an additional contribution to the energy resolution.

- The energy resolution will not scale as $E^{-\frac{1}{2}}$.

- The calorimeter response to hadrons will not be linear with hadron energy.

For achieving accurate energy measurements, especially of hadron jets, each of which may be composed of many hadrons of different energies, each subject to fluctuations in f_{em} and to losses due to interactions involving nuclear breakup, it is therefore desirable to construct a calorimeter that approaches compensation.

Several different phenomena may be exploited to achieve compensation. Using uranium as an absorber, for example, can boost the non-electromagnetic part of a shower through the absorption of any produced neutrons that can induce fission and thereby release energy. The response to the EM part of a shower can be suppressed by taking advantage of the interactions of soft photons. In particular, low-energy photons are absorbed preferentially in high-Z material (the cross section for the photoelectric effect goes as Z^5), and this can reduce the signal observed for the electromagnetic component of a hadronic shower. An important handle on $\frac{e}{h}$ is provided by the response of the sensitive medium to neutrons. For example, an active material containing hydrogen will provide an effective mechanism for the transfer of a large fraction of the neutron's kinetic energy to recoil protons and to ionization of the medium. This mechanism cannot be exploited for calorimeters using only high-Z readout material; however, long signal-integration times can take advantage of the energy released from nuclear capture and break up caused by thermal neutrons. The times scale for the release of γs through this process is on the order of a μs.

2.3 Structure of the D-Zero Calorimeters

The D-Zero calorimeters employ liquid argon as their active media. Advantages of liquid argon over scintillator are: ease of segmentation (light guides and wave shifters are not needed to route signals; this also make it mechanically easier to construct a uniform detector), radiation hardness, and stable gain. A typical unit cell of the calorimeter is shown in Fig 2.4. A grounded metal absorber plate is

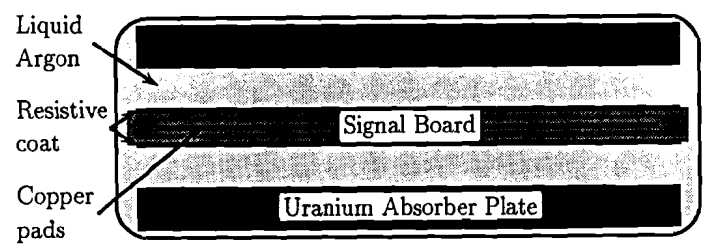

Figure 2.4: Typical Unit Cell in The D-Zero Calorimeter

separated from a signal board by a liquid argon gap. A copper plane, on which readout pads are etched, is sandwiched between two layers of a G-10 insulator. A coating of resistive epoxy on the outer surfaces of the G-10 planes is connected to a positive high voltage (typically 2.0-2.5 kV). Electrons, liberated by shower particles, drift toward the resistive layer on the G-10. This current couples to the signal pads, is eventually amplified, and produces the observed signal. Clearly, any change in the quality of the liquid argon that affects either its ability to transport this ionization (electron) charge, or to produce it will have a direct effect on the observed signal. For example, changes in temperature will affect the density of the liquid and therefore the amount of ionization a particle will produce when traversing the argon layer. Also, any electronegative contaminant, such as oxygen,

present in the argon, which can combine with the electrons before they drift to the positive side of the voltage gap, will reduce the effective signal. Contaminations as low as 1 ppm of oxygen will have a significant effect on the transport of electrons. Appendix A describes in detail the D-Zero liquid argon purity monitoring system used to evaluate argon purity.

The D-Zero calorimeters are composed of three distinct module types: electromagnetic (EM), fine hadronic (FH), and coarse hadronic (CH). In the EM sections, unit cells consists of $\approx 1X_0$ of material, FH sections have $\approx 0.06\,\lambda_{int}$, and the CHs have $\approx 0.3\,\lambda_{int}$. The EM section of the central calorimeter is composed of an annulus of 32 modules. Transverse segmentation is 0.1×0.1 in $\Delta\eta \times \Delta\phi$ for all modules except for the third EM layer (the depth at which EM showers are at maximum), where it is 0.05×0.05. The EM calorimeters are separated into four longitudinal layers of 2, 2, 6.8, and 9.8 radiation lengths, each cell consisting of 3 mm of uranium absorber and two 2.3 mm argon gaps between signal boards and absorber plates. Sixteen fine hardonic (FH) modules surround the EMs. Signals for the FH are read out at three depths, namely after 1.3, 2.3, and $3.1\,\lambda_{int}$. The FH modules use 6 mm uranium plates as absorber. The 16 coarse hadronic (CH) modules that form the third layer of the calorimeter use 46.5 mm copper plates as absorber, with all layers ganged together and read out as a single units. The CH has $2.9\lambda_{int}$ of material.

The two end calorimeters are conceptually similar to the central calorimeter. To avoid dead spaces, a single disk-shaped EM and barrel-shaped hadronic module is used nearest to the axis of the beams. Two layers of hadronic modules encircle these central modules. Figure 2.5 shows the D-Zero central and end calorimeters in greater detail.

In the following chapter we describe the D-Zero test beam and the configuration of modules tested during the 1991 run.

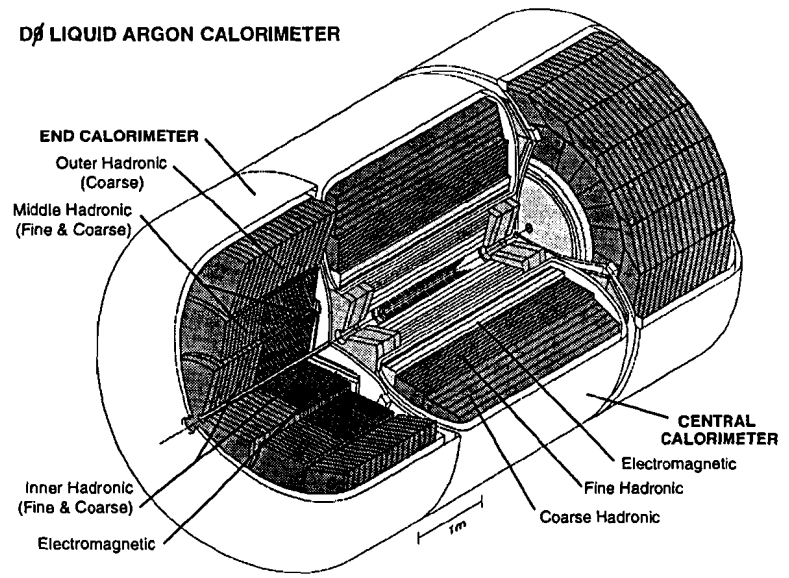

Figure 2.5: Cutaway View of the D-Zero Calorimeters

Chapter 3

The D-Zero Test Beam

The D-Zero experiment has conducted several beam tests of its calorimeter modules [14, 15, 16, 17]. The data presented in this dissertation were acquired between July 1991 and January 1992 at the Neutrino-West (NW) beamline at Fermilab. The D-Zero test beam studies were carried out in NW beamline enclosure A (NWA). During the 1991 run, a replica of a full octant of the D-Zero central calorimeter (CC) was exposed to beams of pions, electrons, and muons in the energy range of 2 through 150 GeV/c. The studies, designed to measure the operating characteristics of the calorimeter modules, included: measurements of energy resolution and linearity of response, position resolution, uniformity and stability of response, and the response of modules at intermodule spaces and near various support structures. In addition, measurements were made of the response of the calorimeter as a function of the high voltage imposed across the argon gaps, and of the effects of mixing certain additives into the liquid argon. Besides the CC modules, several EC modules, as well as a mock-up of the D-Zero intercryostat detector [18], were studied in the test beam. The results presented in this thesis are restricted to measurements performed on modules of the central calorimeter.

3.1 Configuration at the 1991 Test Beam

All the modules studied at the 1991 D-Zero test beam (referred to as "Load-2") were housed within a single liquid argon cryostat. This cryostat was approximately 3m in diameter and 5m long. The modules were placed inside in locations identical to their relative positions in the full D-Zero detector. The cryostat rested on a transporter, as described below. The configuration of central calorimeter modules within the cryostat is shown in Fig. 3.1

3.1.1 CC Modules

Four central calorimeter electromagnetic modules as well as two CC fine hadronic and two CC course hadronic modules were included in the Load-2 configuration. Figure 3.1 highlights the octant of the central calorimeter that was duplicated at the test beam. The material between the colliding beams and the modules that is present in the full D-Zero detector (cryostat walls, central detector, etc.) was simulated by placing a 0.5 inch steel plate and an argon excluder composed of closed cell plastic foam (Rohacell) that was located immediately in front of the EM modules in the test beam cryostat.

3.1.2 The Test-Beam Transporter

The test-beam cryostat was mounted on a motorized, computer-controlled transporter system capable of positioning the cryostat in a variety of positions relative to the fixed beam of particles from the NW beamline. This allowed scanning of the response of modules for particles incident at different positions and at angles identical to those followed by particles from the D-Zero interaction point. Figure 3.2 shows a sketch of the test beam transporter [19]. The transporter was capable of

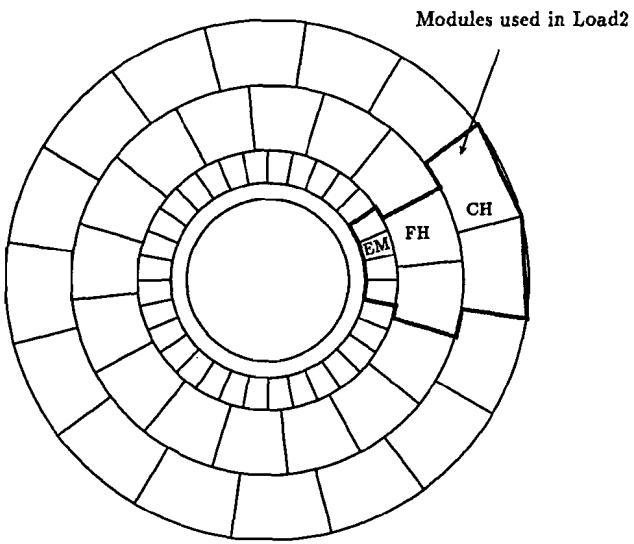

Figure 3.1: Cross section of the D-Zero central calorimeter. The outlined portion represents the octant of the central calorimeter that was duplicated in the 1991 test beam. The innermost ring of modules is composed of electromagnetic modules (EMs), these are surrounded by a fine hadronic (FH) layer and a coarse hadronic (CH) layer.

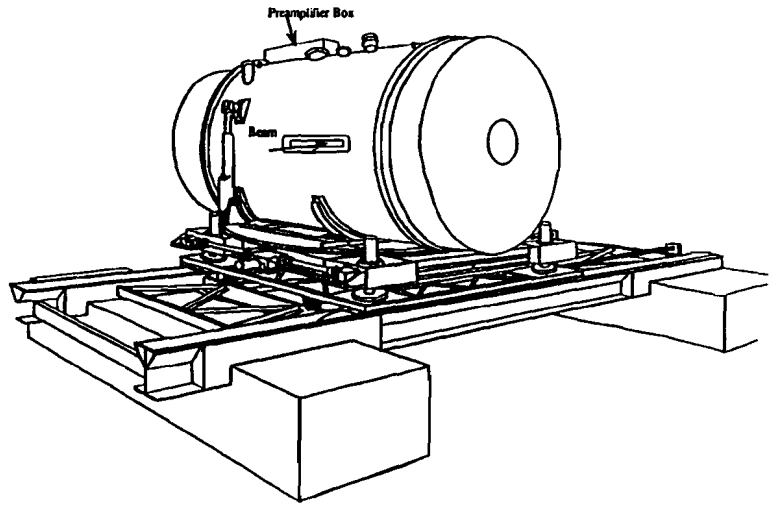

Figure 3.2: Test Beam Cryostat Transporter System

positioning the cryostat within the following range of motion:

- A total of $\pm 190°$ azimuthal rotation about a vertical axis.
- A total of $\pm 15°$ azimuthal rotation about the long horizontal axis of the cryostat.
- A total of 3.5 m horizontal translation perpendicular to the beam
- A total of ± 0.75 m vertical translation relative to the beam center.

3.2 The NW beamline

The NW beamline was used in two configurations during the run of Load-2. Most of the data was collected with the standard (high-energy) configuration. However, for part of the run, the downstream portion of the NW beamline was reconfigured to facilitate the production and transport of low momentum (<10 GeV) particles to the test-beam site.

3.2.1 The High-Energy Configuration

A schematic of the NW beamline is shown in Fig. 3.3. This beamline transported negatively charged particles (e^-, μ^-, π^-) in the momentum range between 10 and 150 GeV/c from a primary aluminum target to the D-Zero test beam area. These particles were produced by colliding 800 GeV/c protons extracted from the Fermilab Tevatron with the target in NW Enclosure 3, located about 580 meters upstream of NWA.

Two double bends (NW4W-NW6E, NW7W-NW9E) in the horizontal plane determined the momentum of the beam. Vertical corrections to the beam position were made using trim magnets, located downstream of each horizontal bend. Two pairs of quadrupole magnets located in NW enclosures 4 and 8 were used to focus the beam.

To produce electron beams, a "sweeper" magnet (NW4S) was used to deflect all charged particles out of the beamline. Photons, being unaffected by this, continued propagating and interacted in a lead target-wheel (NW4PB) to produce electrons, which were then transported along the beamline (similarly produced positrons were swept out of the beamline by the bend magnets NW4W). The purity of the pion beam could be enhanced by placing thin lead targets (≈3 radiation lengths) in the beamline. Electrons radiated in the lead (NW6PB, NW7PB), and

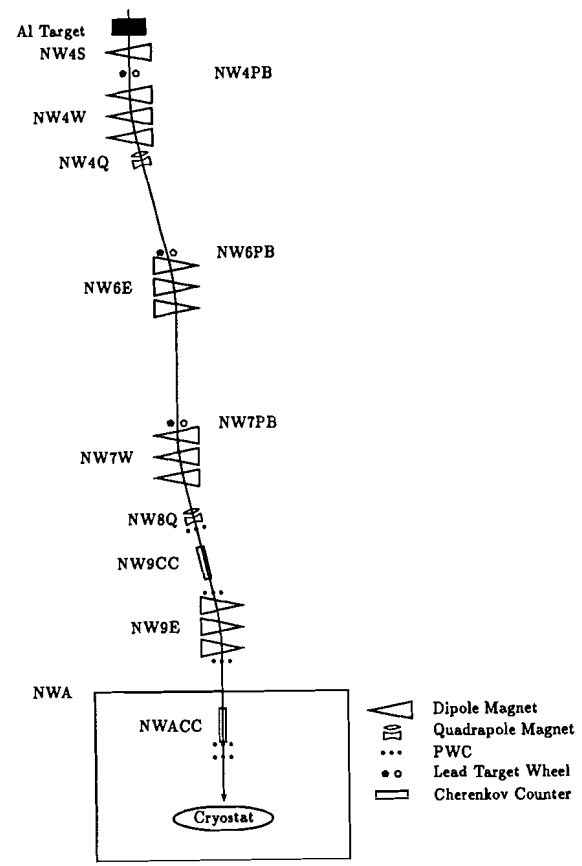

Figure 3.3: High Energy Beamline

quickly fell below the minimum cutoff for transport at a given momentum setting. Magnet currents and target positions were controlled remotely using the Fermilab EPICURE control system [20].

The momentum for each beam particle was calculated from the bend angle measured in the NW9E magnet, using PWC (proportional wire chamber) information both upstream and downstream of the magnet. A particle's momentum can be determined from:

$$p = \frac{B \times L}{517.02 \times sin\,\phi} \tag{3.1}$$

where p is in GeV/c, B is the magnetic field in kilogauss, L the magnet length in cm, and ϕ the full bend angle in radians ($\approx$28 mr for the NW9E magnet). Magnetic field values were determined using a Hall probe located within the NW9E magnet.

3.2.2 Low-Energy Configuration

Due to the relatively short decay length of the lowest energy pions ($\approx$100 m at 2 GeV/c), and because of high beam-transmission losses for particles with momentum $\lesssim$ 10 GeV/c, the standard secondary beamline could not transport a sufficient number of particles below 10 GeV/c. Consequently a beryllium target ($\approx$0.75 m thick), placed 43 meters upstream of the cryostat, was used to create a tertiary beam of particles in the 2 to 10 GeV/c momentum range.

Figure 3.4 shows the changes to the NW beamline for low energy running. A 70-225 GeV/c pion beam was collided with the Be target in NW enclosure 8. An additional horizontal bend magnet (NW8E) was added downstream of the target to select particles at an angle of 8 mr. Also, several quadrupole elements were added to the beamline to improve the focus of the tertiary beam. Pions that punched through the target were stopped in the steel beam dump placed downstream of NW8E. No particle selection was possible in the tertiary beam, so all tertiary beam

running consisted of mixed species of electrons, pions, and muons. Selection criteria used for distinguishing these particles are described in the following chapter.

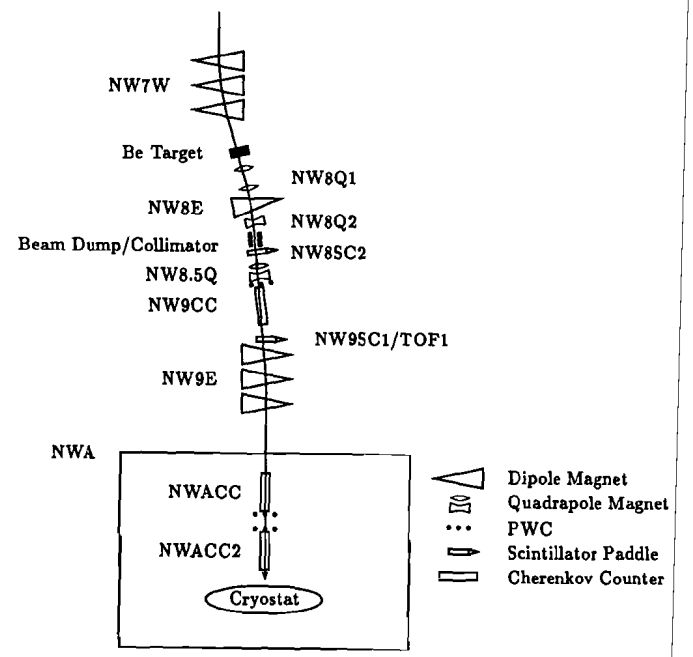

Figure 3.4: Low Energy Beamline

Chapter 4

Energy Response of the D-Zero Central Calorimeter

This chapter presents the response of the D-Zero central calorimeter at η=0.05 ($\approx$ 90° to the beam axis) and ϕ=3.16 radians (3.375° below the beam axis), as obtained from the studies at the D-Zero Test Beam. The energy scale and resolution of the calorimeter were obtained over the range of energies from 2 through 150 GeV, for both pions and electrons. As we will discuss in Chapter 5, the response of a calorimeter to low energy particles has major impact on its response to high energy jets produced in the hard scattering of partons, which are composed typically of a large number of relatively low energy particles ($\lesssim$ 10 GeV).

4.1 Systematics

The observed (uncorrected) response of the CC modules to low energy particles can be affected by various sources of systematics. For example, possible momentum offsets due to incorrect values of magnetic fields used for the bend magnets (from small offsets in field measurements), and varying of muon contamination in the

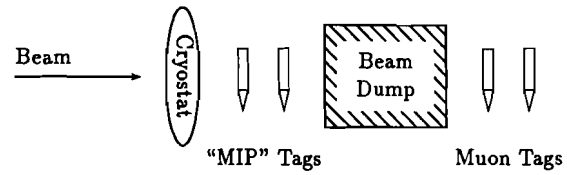

Figure 4.1: Arrangement of scintillator tags downstream of the calorimeter for the detection of energy leakage. MIP refers to a minimum ionizing particle.

pion sample due to inefficiencies in pion and muon identification, can produce shifts in response. Such systematic effects did not significantly affect higher-energy data. Although a careful study of the effects of any systematic errors on our momentum measurements is currently underway, the momentum uncertainty of the secondary (higher-energy) beam was assumed to be less than 1% [21, 22]. (Recent studies indicate that offsets on the momentum measurements were no greater that 0.5% [23].) Also, scintillators located behind a steel beam dump downstream of the calorimeter tagged high energy muons (see Fig. 4.1), and simple criteria imposed on the longitudinal energy deposition were useful in separating pions from muons. However, because of multiple scattering and a decrease in the signal to noise ratio for pions, discrimination against muons was poor for energies below 7.5 GeV. At such low momenta, muons and pions were identified by a threshold Cherenkov counter (see below).

4.1.1 Cherenkov Leaks and Pressure Offsets

Muons were distinguished from pions using a 6 m threshold Cherenkov counter, filled with freon-114, that was located immediately upstream of the test beam cryostat (NWACC2 in Fig. 3.2.2). The counter was usually operated near the

threshold for pions, and consequently only muons (or electrons) provided cherenkov signals at the nominal beam momentum. The gas pressure in this device was measured using a Wallace & Tiernan (W&T) mechanical pressure gauge.

Also, during the run, a slow leak was detected in the freon Cherenkov counter, the effect of which would be to contaminate the freon with air, especially for operation below atmospheric pressure, but also to produce a drop in pressure for runs above atmospheric pressure. The leak rate was measured to be approximately 0.008 psi/hr. The effect of the leak on Cherenkov operation was considered small enough to be ignored. The leak rate was slow compared to the rate of data taking, and periodic refilling of the counter maintained a relatively constant gas pressure and quality.

4.1.2 Momentum Distributions and Muon Contamination

Because all species of particles (e, π, μ) were transported down the same beamline, it would be reasonable to assume that the momentum distributions of all the species should be the same. Nevertheless, this is not found to be the case. For all the data in the momentum range between 2-5 GeV/c we observe that the muon spectra are shifted above the nominal value of momentum, and the 2, 2.5, and 3 GeV/c pion data display a small shift to below the nominal value of momentum. Figure 4.2 shows the observed momentum distributions for tagged pions, muons and electrons at nominal beam momenta of 2 GeV/c and 5 GeV/c.

The observed shifts are consistent with the assumption that, for nominal settings, at highest momenta pions can trigger the Cherenkov counter and be misidentified as muons, while at lowest momenta muon momenta may fall below values where the counter is fully efficient and thereby be misidentified as pions. The observed shape of the pion momentum distribution will therefore be like the electron

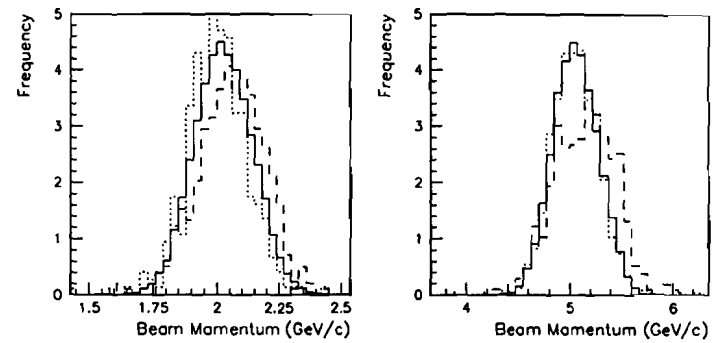

Figure 4.2: Momentum distributions for 2 GeV/c (left) and 5 GeV/c (right) particles. Solid lines correspond to tagged electrons, dotted lines to tagged pions, dashed lines to tagged muons.

distribution, but with a reduced high-momentum component, and an enhanced low-momentum component, due to misidentification at pion and muon Cherenkov thresholds. In addition, because of inefficiency of the Cherenkov counter ($\lesssim 2\%$), a small fraction of muons will never yield a trigger, and will thereby be misidentified as pions.

To estimate the muon contamination in each low-energy pion sample, the pion and muon spectra were fitted simultaneously using the following functions:

$$\mathcal{N}_\pi(p) = N_\pi P_e(p)(1 - f \cdot E_\pi) + N_\mu P_e(p)(1 - f \cdot E_\mu) \quad (4.1)$$

$$\mathcal{N}_\mu(p) = N_\pi P_e(p)(f \cdot E_\pi) + N_\mu P_e(p)(f \cdot E_\mu) \quad (4.2)$$

where $\mathcal{N}_\pi(p)$ is the observed momentum distribution for particles tagged as pions, $\mathcal{N}_\mu(p)$ is the observed distribution of tagged muons; $P_e(p)$ is the shape of the momentum spectrum obtained from the electron sample (normalized to one

event); p is momentum; $N_{\pi(\mu)}$ corresponds to the true number of pions(muons) in the data sample, and the function $E_{\pi(\mu)}$ represents the Cherenkov "turn-on" function for pions(muons) as a function of their momentum, namely the probability that a pion(muon) of a given momentum will produce an acceptable signal in the counter. $N_\mu P_e(p)(1 - f \cdot E_\mu)$ represents the muon component contaminating the observed pion sample, where f is the maximum efficiency of the Cherenkov counter (well after turn-on). The electron momentum distribution at each energy was parametrized by a sum of two gaussian functions, which provided excellent fits to the data. The turn-on functions were characterized as follows:

$$E_\pi = 1 - exp(\alpha(p - p_\pi)) \qquad E_\mu = 1 - exp(\alpha(p - p_\mu)) \tag{4.3}$$

where $p_{\pi(\mu)}$ are threshold momenta in GeV/c for Cherenkov tagging of pions(muons) at any given pressure. The values of N_π, α, p_π, and p_μ were allowed to vary in the fits. However, since the muon momenta were well above threshold, the fits were insensitive to p_μ. Using two upstream helium-filled Cherenkov counters to tag electrons, and then comparing this tag to signals from the freon Cherenkov, the value of f was determined to be $0.980 \pm .005$.

Figure 4.3 shows a fit to the 4 GeV/c pion and muon momentum spectra. An estimate of the muon contamination in the pion sample is obtained from such fits to Eq. 4.1, the results of which will be summarized in Table 4.2 at the end of Section 4.1.4.

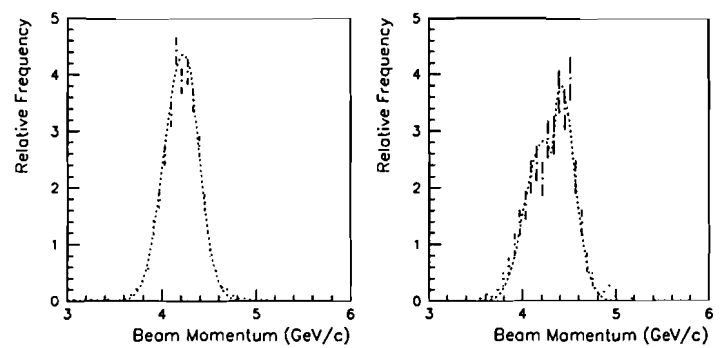

Figure 4.3: Fits to pion and muon momentum distributions. The nominal beam momentum is 4.25 GeV/c, the pion distribution is shown on the left and the muon distribution on the right.

4.1.3 Momentum Offsets

An asymmetry of the kind displayed in Fig 4.3 is observed in the muon momentum distributions at each beam momentum between 2 and 5 GeV/c. This feature, incorporated into Eq. 4.1, corresponds to the contribution from pions, of sufficiently high momentum, that trigger the freon Cherenkov counter (i.e., provide a muon signal). The parameter p_π, representing the threshold value in the fit to the data affects this asymmetry. In principle, the value of p_π can be calculated from the index of refraction of the gas in the counter. The dependence of p_π on pressure for freon-114 is given by the relation [24]

$$p_\pi = \sqrt{102.3/P} \tag{4.4}$$

where P is the gas pressure in psia.

As we discuss below, the threshold values obtained from the fits (Table 4.1) do not agree with the expected values at lowest momenta. This seems to imply that either our momentum measurements or our pressure measurements are in error. Pressure measurements would require offsets of over 3 psi to explain the discrepancies in p_π. However, an offset of about 150 MeV/c in the momentum measurement agrees well with the 2-3 GeV/c data. This would correspond to an offset of less than .1% of the dynamic range of the Hall probe used in measuring the fields of the bending magnets in the NW beam. It was, unfortunately, not possible to calibrate the probe at the lowest magnetic fields, and this is the reason we also fitted for values of p_π, which are listed in column 2 of Table 4.1. The fourth column in Table 4.1 shows the offset in freon pressure that would be required to account for the shift from the expected value of p_π. It is unlikely that our pressure

Table 4.1: Thresholds for Cherenkov Radiation for Pions

Nominal Momentum (GeV/c)	Fitted p_π (GeV/c)	Expected Value of p_π (GeV/c)	Implied Offset in Freon Pressure (psi)
2.0	1.999±0.027	2.14	3.2
2.5	2.482±0.034	2.61	1.6
3.0	3.015±0.016	3.12	0.7
4.0	4.315±0.011	4.34	0.1
5.0	5.152±0.027	5.17	0.0

offsets could have been this large, and certainly not possible that they would have changed with beam momentum. A possible explanation for these results is the presence of an offset or non-linearity in the Hall probe. This would correspond to a 7% departure from linearity in the probe at 100 Gauss (the magnet setting for the 2 GeV/c beam). However, such an offset should also be evident in the fits to the 4 and 5 GeV/c data. Figure 4.4 shows the ratio of readings in the Hall probe to the

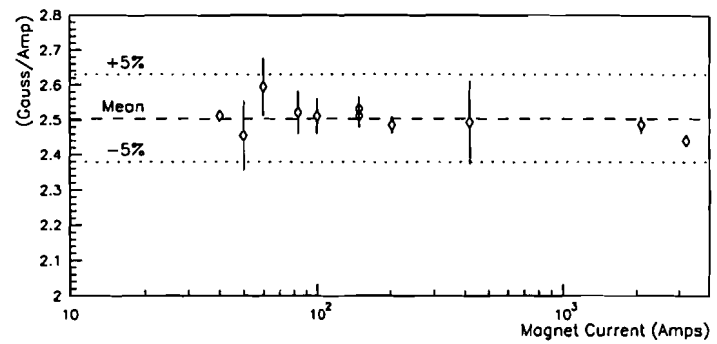

Figure 4.4: Ratio of Hall probe reading to magnet readback current versus magnet readback current.

magnet readback current, versus the readback current (i.e., from the bend magnets used for setting the beam momentum). The data does not appear consistent with a 7% deviation from linearity at 40 amps (100 Gauss). We will therefore present the data without implementing any correction for momentum mismeasurement at values ≤ 3 GeVc, and will use the fitted values of p_π as ad hoc parameters. Because the muon backgrounds are very small, this source of uncertainty does not have a great impact on our corrections for muon contamination.

4.1.4 Corrections to the Low Energy Data

From the results of the fits to the pion and muon momentum distributions, we can calculate corrections to the observed calorimeter response for pion momenta of 2 through 5 GeV/c. In particular, assuming the admixture of distributions determined by the fits of Eqs. 4.1 and 4.2 to the data, we extract the correction for muon contamination by comparing the response of pions and muons from the

Table 4.2: Corrections to the observed pion signals at low energy

Momentum (GeV/c)	Muon/Pion Energy Response	Muon Contamination	Correction for Muon Contamination
2.0	1.56±.03	2.23±.13%	0.9877±0.0007
2.5	1.26±.02	1.30±.22%	0.9966±0.0006
3.0	0.99±.01	1.78±.48%	1.0002 ± < 0.0001
4.0	0.72±.01	0.36±.02%	1.0010 ± < 0.0001
5.0	0.58±.01	0.23±.01%	1.0010 ± < 0.0001

Plate-Level TB Monte Carlo simulation of the detector using the CERN program GEANT [25, 26]. Column 2 of Table 4.2 shows the expected relative response of the calorimeter to pions and muons of same momenta as determined from the Monte Carlo [27]. The extracted muon contamination is given in column 3, and is essentially consistent with the expected values of the observed inefficiencies of the freon Cherenkov counter (that is, $1 - f$) at the different settings. Table 4.2 also summarizes the small corrections applied to the pion energy response at low momenta.

4.2 Data Selection and Energy Response

Before presenting the results of energy scans and fits to the resolution, we discuss the criteria we used to select the data in the sample. For the whole data set, we attempted to keep the selection criteria as simple and uniform as possible. Nevertheless, variations in beam conditions during the runs will necessitate some local adjustment of selection criteria.

4.2.1 Selections Applied to All Data

Particles that triggered both helium Cherenkov counters in the NW beamline (NW9CC and NWACC) were labeled as electrons. The response of the calorimeter was examined as a function of position of entry, as determined from PWC tracking chambers. In order to avoid complications due to gaps between calorimeter modules, and scraping of beam particles in upstream material, cuts limiting the beam spot in X and Y (horizontal and vertical dimensions) were applied to all data. However, for pions of momenta of $\lesssim 5\,\mathrm{GeV/c}$, low tracking efficiency (the tertiary beam was not well focused), combined with the small size of the data sample made it too restrictive to require tracking in the Y-direction as well as in X. Consequently, for low beam momenta, an acceptance criterion was based on the average value of ϕ, as obtained from the cells of maximum energy in each of the first seven layers of the calorimeter. This mean ϕ_{max} was required to be in the range $3.08 \leq \phi_{max} \leq 3.20$ radians, roughly in the center of an EM module. Pion energies were reconstructed using a sum over a 7x7 cell road in η and ϕ, taken over all eight layers of the calorimeter. Electron energies were obtained using a sum over a 5x5 cell road for the first 5 layers. Only those events that had well reconstructed beam tracks in the X-views of PWCs were selected for study, and the observed signals were normalized to the measured beam momentum, after the subtraction of "in-spill" pedestals for all the summed electronics channels. In-spill pedestals were determined by sampling the calorimeter's response at random trigger intervals during the data taking (beam spill time).

4.2.2 Additional Criteria for Low Energies

Because the tertiary beam had substantial backgrounds, a scintillator tag in NW Enclosure 8 (after the collimator), and another scintillator tag in NW Enclosure 9 (before the last bend magnet), were required to verify that the particle in question propagated through the beam vacuum pipe. As discussed above, a freon Cherenkov was used to discriminate pions from muons for momenta between 2 and 5 GeV/c. Since the pressures in this counter were set somewhat above the pion threshold, the rejection efficiency for muons was excellent, which provided a relatively clean pion sample at the expense of labeling a significant fraction of pions as muons. It was also possible, however, to obtain clean samples of muons by requiring that each beam particle tagged as a muon had a momentum below the fitted value of p_π discussed in Section 4.1.2.

4.2.3 Criteria for High Energies

As mentioned in Section 4.1, high energy muons ($\geq$7.5 GeV) were tagged using scintillators placed downstream of a steel beam dump, located immediately behind the cryostat. However, because of inefficiencies in the counters and much multiple scattering, especially at energies under 15 GeV, a fraction of the muons did not produce signals in these counters. The character of the longitudinal energy deposition in the calorimeter was therefore used to help reject muons. In particular, it was required that a pion have a signal at least ten times the expected RMS noise level in at least one layer within a 3x3 cell road. The low-energy, minimum ionizing muons failed to pass this criterion, whereas pions did not. (This ignored muon radiation and pion punch through, both of which would not be important at low energies.) The distributions in energy deposition for muons and pions were well separated at energies greater than 20 GeV (not shown).

The central calorimeter is 7.1 nuclear interaction lengths deep at (90°), and for a fraction of high energy pion showers, some energy escapes the calorimeter. Section 4.4 describes the effects of longitudinal leakage on calorimeter response. The pion response at high energy was obtained by requiring no "punch through", namely no signal in either of the two scintillation counters located immediately downstream of the cryostat (see Fig 4.1). This requirement improves the resolution for pions, but, clearly, cannot be easily employed in D-Zero.

4.2.4 Linearity of Calorimeter Response

The energy response of the calorimeter to electrons and pions between 2 and 150 GeV/c is plotted in Fig. 4.5. The values correspond to the means obtained from gaussian fits to the calorimeter's response at each energy. Also shown in Fig. 4.5 are residuals from a linear fit to the data ($(fitted - measured)/fitted$) for both pions and electrons. The large residuals observed at lower energies represent non-linearities in response. It is likely that the discrepancy for electrons arises because such low-energy particles lose energy in the uninstrumented material upstream of the first electromagnetic sampling layer, and this loss is not properly compensated by the sampling fractions* applied to the reconstruction of energy (i.e., the sampling is too coarse at these energies). The calorimeter provides a linear response of better than 1% to electrons in the energy range between 4 and 150 GeV. The response to pions is linear to within 2% down to 10 GeV.

Table 4.3 summarizes the values obtained from gaussian fits to the energy responses of the calorimeter to electrons and pions for both the tertiary beam (low-

*For a given calorimeter layer consisting of absorber and active layers, the sampling fraction represents that fraction of a particle's energy deposited in the active medium. The energy of an incident particle is reconstructed by summing the energy in each layer after dividing by the sampling fraction.

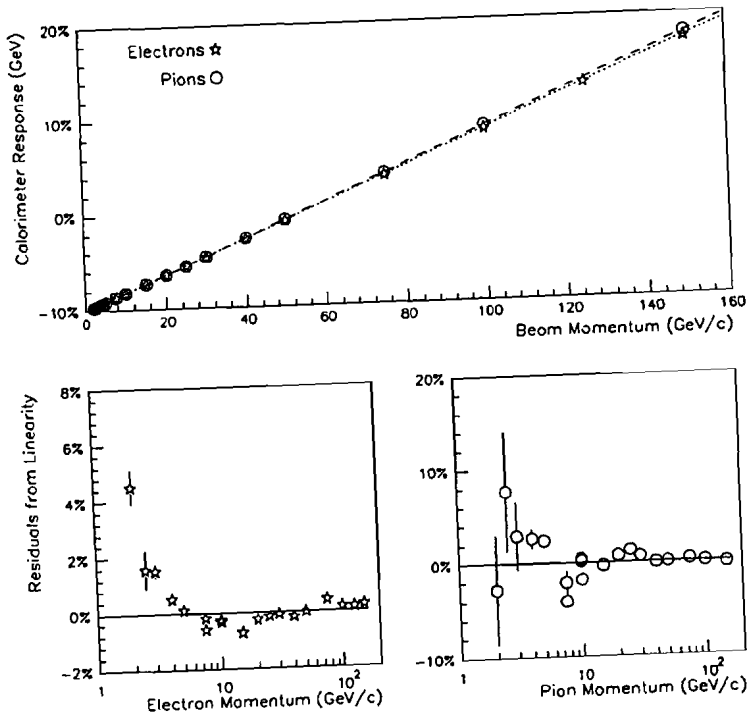

Figure 4.5: Calorimeter response to pions and electrons for 2 through 150 GeV/c. (Fits can be parametrized as: Electron Response(GeV) $= 0.978 \cdot \mathbf{p} - 0.077$ GeV, Pion Response $= 0.996 \cdot \mathbf{p} - 0.537$ GeV.)

energy) data and the secondary beam (high-energy) data. The results are given before the application of the small muon corrections discussed in Section 4.1.4. These corrections were applied, however, to all the pion data of 2 through 5 GeV energy presented in the figures of this chapter.

Table 4.3: Reconstructed Energies (without small corrections for muon contamination)

Reconstructed Energy in GeV (Tertiary Beam)				
Beam	Electrons		Pions	
Momentum	E	σ	E	σ
2.0	1.79±0.01	0.476±0.012	1.51±0.09	1.28±0.07
2.5	2.33±0.02	0.469±0.012	1.81±0.12	1.34±0.11
3.0	2.81±0.01	0.466±0.005	2.38±0.09	1.49±0.05
4.0	3.81±0.01	0.492±0.005	3.35±0.03	1.49±0.04
5.0	4.81±0.01	0.521±0.002	4.33±0.02	1.68±0.00
7.5	7.27±0.01	0.557±0.006	7.22±0.03	1.77±0.02
10.0	9.73±0.01	0.570±0.011	9.59±0.03	1.99±0.02
Reconstructed Energy in GeV (Secondary Beam)				
7.5	7.30±0.01	0.570±0.007	7.08±0.08	1.65±0.05
10	9.73±0.01	0.571±0.002	9.39±0.03	1.87±0.02
15	14.69±0.01	0.681±0.003	14.46±0.06	2.21±0.06
20	19.53±0.01	0.719±0.013	19.26±0.07	2.54±0.06
25	24.40±0.01	0.791±0.017	24.06±0.05	2.99±0.04
30	29.28±0.01	0.859±0.009	29.17±0.04	3.23±0.03
40	39.10±0.02	0.965±0.010	39.33±0.05	3.82±0.03
50	48.81±0.02	1.05±0.01	49.27±0.07	4.45±0.09
75	72.95±0.04	1.18±0.03	73.98±0.18	5.50±0.18
100	97.54±0.06	1.38±0.05	99.07±0.13	6.31±0.14
125	122.0±0.05	1.47±0.04	-	-
150	146.3±0.06	1.66±0.06	149.1±0.08	8.95±0.16

4.3 Energy Resolution of the Calorimeter

The measured energy resolution of the calorimeter is shown in Fig. 4.6. The measured fractional energy resolutions σ/E, where σ and E are the standard deviations and means from gaussian fits to the calorimeter's energy response can be parametrized as follows:

$$\frac{\sigma}{E} = \left(C^2 + \frac{S^2}{E} + \frac{N^2}{E^2}\right)^{\frac{1}{2}} \tag{4.5}$$

where E is the average energy measured in the calorimeter in GeV, C is a constant contribution to the resolution from systematic errors such as detector non-uniformities and channel-to-channel gain variations. S is the statistical error in the sampling, and N represents energy independent contributions to noise (e.g., pedestal fluctuations and noise signals from radioactive decays of the uranium absorber). In all the fits, N was fixed to the total pedestal width for the cells included in the energy measurement.

4.4 Longitudinal Leakage at High Energy

Figure 4.7a shows the measured probability, as a function of incident pion momentum, for the detection of energy leakage downstream of the Test Beam cryostat, as determined using either of the two scintillator paddles (MIP tags) sketched in Fig. 4.1. Also shown in Fig. 4.7a is the probability that an event that exhibits leakage will deposit energy that is at least two standard deviations below the nominal value obtained for particle showers that do not trigger the scintillator detectors. Figure 4.7b shows the percent shift in the average response for all data (including events with leakage) relative to data selected to have longitudinal containment.

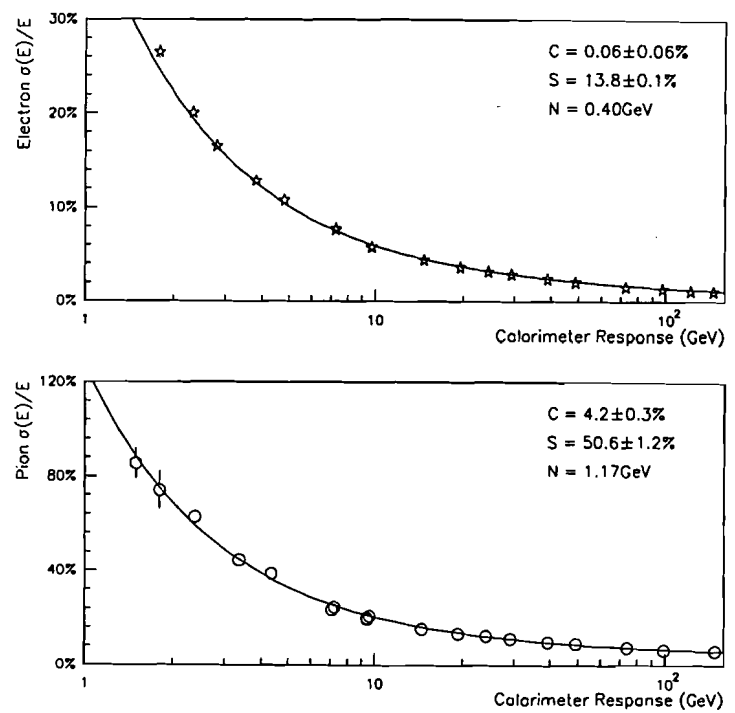

Figure 4.6: Fits to the energy resolution for electrons and pions of momentum between 2 and 150 GeV/c

The mean calorimeter response is reduced significantly for incident pions with momentum above 40 GeV/c. In particular, the typical response for 150 GeV/c pion data is seen to decrease by about 1.5%. In Fig. 4.8, the response to 150 GeV/c pions is shown both with and without events that are not completely contained in the calorimeter.

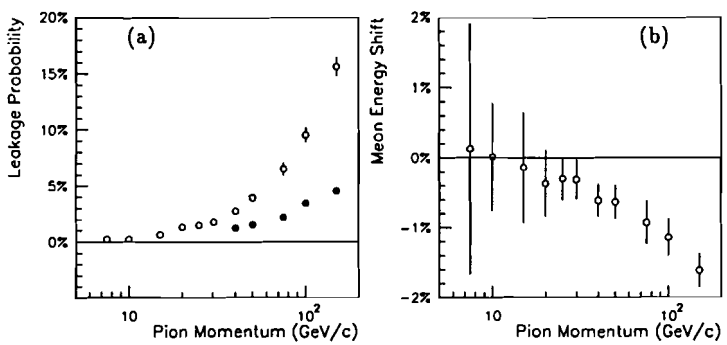

Figure 4.7: Leakage effects for high energy pion showers. (a) Probability for a pion shower to punch through the CC at η=0.05 (circles). Solid circles represent the probability that an event that has leakage will have an energy at least two standard deviations below the most probable value obtained for fully contained showers. (b) Ratio of the mean response for all data to that for completely contained pion showers.

It should be emphasized that the calorimeter response presented thus far is for an idealized performance in that only fully contained showers were used in the analysis. In general, an improvement in resolution, for arbitrary showers (independent of leakage), can be obtained using an H-matrix formalism [28], but this was not attempted. It is useful, however, to model the response of the calorimeter to take rough account of the effects of longitudinal leakage. We did this for pion data from 40 through 150 GeV/c by fitting a sum of three gaussians to all data.

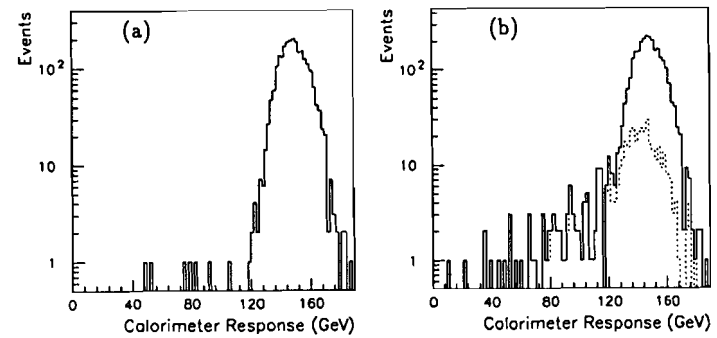

Figure 4.8: Pion response at 150 GeV/c. (a) Calorimeter response for events with no detectable leakage. (b) Calorimeter response for all events. The dotted distribution is for events that have leakage that is detected using the downstream scintillator paddles.

This crude parametrization offers a good representation of the low-energy tails observed for the pion energy distributions. The mean of the averaged functions agrees with the means of the data to within 0.5% accuracy. The results of our fits are summarized in Table 4.4. However, an improved parametrization will certainly be required for a detailed study of leakage effects in the D-Zero experiment.

In the following chapter we consider the impact of the response of the calorimeters to low energy particles on the reconstruction of jets of hadrons.

Table 4.4: Parametrization of events with leakage to a sum of three gaussian functions of the form: Const $\times \exp[(E - \text{Mean})^2/2\sigma^2]$.

Momentum	Gaussian 1			Gaussian 2			Gaussian 3		
GeV/c	Const	Mean	σ	Const	Mean	σ	Const	Mean	σ
150	213.12	148.30	8.9095	2.4623	130.25	36.611	1.1053	32.774	41.318
100	175.58	98.712	6.6403	2.0445	83.158	41.402	0.6276	6.5199	11.563
75	153.78	73.825	5.4031	2.4052	71.458	25.662	1.0133	12.160	12.425
50	313.22	49.169	4.3606	3.8309	45.329	17.042	1.1160	10.580	5.2301
40	372.57	39.281	3.7723	3.7173	33.193	17.217	1.2593	3.8845	0.7058

Chapter 5

Correction of the Energy-Scale for Jets Using Data from the Test Beam

5.1 Introduction – Effect of Response to Low-Energy Particles

An accurate understanding of the response of the D-Zero calorimeters to hadronic jets is crucial for making precision measurements of jet production and testing QCD. Because jets are composed of many particles, each of which carries only a fraction of the total energy of the parton, the response of the calorimeter to incident jets is effectively the sum of its response to the individual particles that constitute the jets. For example, it is known that on average, 67% of the total energy of a 50 GeV jet is carried by particles with energies below 5 GeV [29], and it is still a substantial 40% for 150 GeV jets. Thus, relatively low energy particles tend to dominate the fragmentation of jets produced at the Tevatron. Any non-linear

response of the calorimeter to low-energy (< 10 GeV) particles is therefore bound to have a particularly derogatory effect on reconstruction of jets. As we showed in Chapter 4, the response of the D-Zero calorimeter to low-energy electrons and pions differs substantially. This leads to uncertainties in the measurement of jet energies. The fraction of particles in a jet that interact electromagnetically varies from jet to jet, and therefore the jet composition (each particle type) must be known in order to correct the jet response for such variation. Current detectors usually cannot identify all the particles in jets. Consequently, uncertainties in parton fragmentation limit the ability of applying corrections due to non-linear response at low energies on a jet by jet basis. Nevertheless, a global correction can be applied that provides a correct response, at least on average.

5.2 Other Systematics

Other factors may contribute to systematic uncertainties in the measurement of the energy of jets, such as non-uniformities in the detector that cause an uneven energy response from one section of the detector to another. Uninstrumented material, such as intermodule spacers and cryostat walls, can cause mismeasurement of energies. Other uncertainties arise from algorithm-dependent effects (e.g.,"clustering effects") in jet reconstruction. The energy of a jet is defined typically to be the energy within a cone about the axis of the jet. In D-Zero, we often use a cone of radius $R = \sqrt{\Delta\phi^2 + \Delta\eta^2} = 0.7$ to define jets. Some energy may leak outside of this cone, or, alternatively, particles from another jet may leak into it. Problems may also arise from closely spaced jets being merged into single jets. Figure 5.2 shows the estimated contributions of the above effects to the systematic uncertainty in jet energy, as reported by the CDF experiment [30].

The response of a calorimeter to jets of a given energy, or the "jet energy

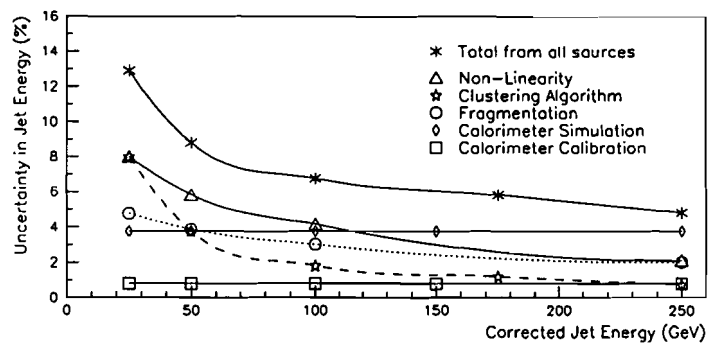

Figure 5.1: The systematic uncertainty in measurement of jet energy for the CDF experiment. Contributions from different sources are shown separately and all added in quadrature.

scale", must be understood, particularly for obtaining accurate measurements of jet phenomena that vary rapidly with jet energy, such as the inclusive jet cross section (see Fig. 5.2). Because of the steep $\approx E_T^{-5}$ behavior, a 1% measurement error in the jet transverse energy will correspond to about a 5% error in the single-jet inclusive cross section [31].

5.3 Application of Data from the Test Beam

A preliminary study was conducted for applying single-particle responses measured at the D-Zero test beam to obtain the response for jets in the D-Zero central calorimeter by A. Milder and R. Astur [29]. The following procedures were used:

- Jets of particles in the energy range of 20 to 200 GeV were produced using the Monte Carlo event generators, Pythia [33], Herwig [34], or ISAJET [35].

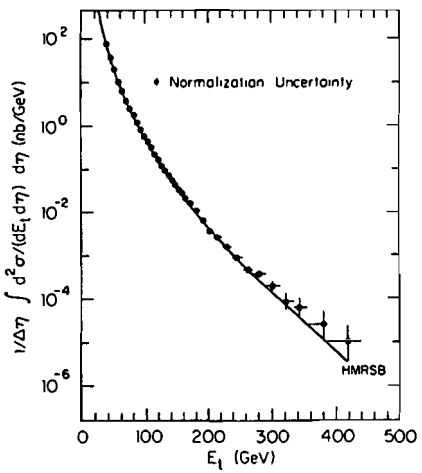

Figure 5.2: Inclusive E_t spectrum for a cone size of $R = 0.7$, averaged over the pseudorapidity interval $0.1 \leq |\eta| \leq 0.7$ from CDF measurements at $\sqrt{s} = 1.8$ TeV [32].

The energies and directions of the particles composing the jets were obtained.

- Jet energies were defined by forming energy-weighted centroids from particles emitted within a cone of radius $R = 0.7$ relative to the jet axis. Starting with the particle of largest E_T iterations were made about the initial axis, until a stable solution was obtained that contained all the particles within $R = 0.7$.

- The energy of each specific particle within the cone of acceptance was divided by the correction factor for response measured at the test beam. Highest energy particles (150 GeV) were defined to have a full response, this correction factor increased with decreasing energy due to non-linearities in the response of the calorimeter. Figure 5.3 shows the effective drop in response used for electrons and pions as a function of energy, as measured using the test beam data presented in Chapter 4. To summarize:

  - The response to electrons and photons was multiplied by the correction factor found for electrons at the test beam. (Because of the material in front of the first electromagnetic sampling layer, the correction should not be as large for photons as for electrons, but this small expected difference was ignored.)

  - π^0s and η^0s were treated as if they decayed into two photons, each with half the energy of the original particle. (This is correct on average.)

  - All other particles were taken as hadrons, and were divided by the correction to the response observed for pions at the test beam.

  - The response for particles showering near intermodular cracks was downgraded by an appropriate amount, again, as measured in test beam studies.

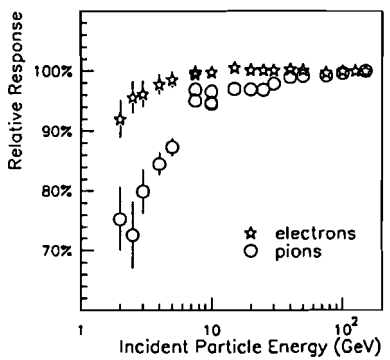

Figure 5.3: Energy response of D-Zero central calorimeter to electrons and pions relative to the response at 150 GeV.

5.4 Extraction of Corrected Response to Jets

The ratio of the mean modeled response relative to the energy generated for the jets, based on the procedures described above, is shown in Fig. 5.4. Also shown in Fig. 5.4 is the inverse, namely, the correction factor for the observed energies of jets in the calorimeter. The upper and lower error estimates were generated by shifting the responses in the test beam up or down by one standard deviation and by adding in quadrature factors representing the uncertainties in energy scale between signals from the test beam and those from the D-Zero calorimeter.

Clearly, there are many limitations to this correction technique. For example, effects from loss of shower particles beyond the defined cone size (i.e., wide pion showers may extend beyond the cone), and the effects of zero-suppression of signals in individual calorimeter cells, were not implemented properly. A more detailed investigation of the response of the central calorimeter to jets that will use test-

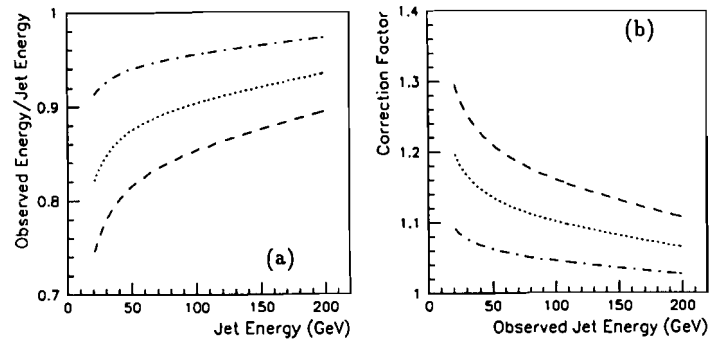

Figure 5.4: Estimated response of the D-Zero central calorimeter for jets in the energy range of 20-200 GeV (a). Correction factor for observed jet energies (b). In each plot the dashed and dot-dashed lines represent upper and lower error estimates on the correction factors [29].

beam data for providing energy distributions of particles in individual the cells is under way and will incorporate a more realistic calorimeter response [19].

In the remaining chapters we consider the effects on the energy response of additives mixed in with the liquid argon, and the effects of altering the charge collection voltage on the D-Zero calorimeters.

Chapter 6

Studies of Effects of Additives and Corrections to Calorimeter Response

The effects on the response of the D-Zero central calorimeter from the admixing of various additives to the liquid argon were studied at the conclusion of the 1991 test-beam run. Five gaseous samples were added in turn, and the response examined for both pions and electrons in the energy range of 10 through 150 GeV/c. Table 6.1 summarizes the relative concentrations of different gasses mixed into the argon volume of the cryostat. The argon was not changed between consecutive additions of material, and consequently all effects are cumulative.

The measurements after addition of oxygen can be used to correct the responses of D-Zero calorimeters for any signal degradation due to oxygen contamination of the argon, as well as to relate the responses of the calorimeters according to the quality of the argon purity in each cryostat. The presence of oxygen in the liquid argon suppresses the observed signal. The oxygen captures a fraction of

Table 6.1: Additives to liquid argon during 1991 test beam run

	Additive	Approximate Concentration in Calorimeter
1	Oxygen	1 ppm
2	Oxygen	1 ppm
3	Nitrogen	4 ppm
4	TMG[a]	2 ppm
5	Nitrogen	100 ppm

[a] tetramethylgermanium ($Ge(CH_3)_4$)

the ionization electrons, thus reducing the total charge which drifts to the anode planes in the calorimeter. While nitrogen is known to have a weaker effect on charge collection in liquid argon [36], a small amount was added after the second dose of oxygen so as to simulate more closely the composition of air, which is a more likely contaminant of the argon than just oxygen alone.

TMG is a photosensitive compound that can increase the charge collection efficiency in liquid argon by decreasing saturation of signal for densely ionizing tracks. Scintillation light from recombination of electrons and argon ions can be converted by TMG molecules into photoionization produced a small distance away from the original region of ionization. In general, such electrons will be far less likely to undergo recombination [37], and thereby enhance the signal. TMG was added therefore to determine its relative effect on electron and pion signals in the calorimeter, and to test whether it could be used as a tool for equalizing hadron and electron response in liquid argon calorimeters. The addition of the large amount of nitrogen was also done to determine any differential effects on the response of the calorimeter to pion and electron showers. Nitrogen preferentially suppresses signals from heavily ionizing particles by limiting the mobility of electrons [38], thus increasing their drift time and thereby the probability for recombination.

Consequently, its effect is opposite to that of TMG. In this chapter we concentrate on the effect of oxygen contamination, and on the corrections to the response based on our measurements using the D-Zero argon-purity monitors.

6.1 Response of D-Zero Argon Purity Monitors to Additives

The D-Zero argon purity monitors reflect the efficiency of transporting ionization in the liquid argon of each D-Zero cryostat. The monitors consist of two ionization cells, one containing an ^{241}Am α source (the "α" cell) and the other a ^{106}Ru β source (the "β" cell). These sources ionize the liquid argon in their vicinity, and the liberated electrons are collected via an adjustable high voltage plane (anode) located above each source. The response of the monitors, as measured by the ionization charge that drifts to the anode, is sensitive to the purity of the liquid argon. Signals are reduced by any electronegative contaminant in the argon that can capture the ionization electrons. Appendix A contains a full description of the D-Zero argon purity monitors and details concerning their operation.

The responses of an α cell and a β cell, used in the test beam calorimeter, are displayed as a function of time, respectively, in Figs 6.1 and 6.2. Figure 6.1 shows the response at charge collection voltages of 13 kV/cm and 4.3 kV/cm, before and during the additive studies. Large drops in signal are observed after each addition of oxygen. The inset graph, showing the effect of adding 4 ppm of nitrogen, indicates only a relatively minor change in the response of the α cell. In fact, at 13 kV/cm, the change in α response due to the addition of nitrogen was $\approx$40 times smaller that that produced by an equal amount of oxygen. The effect of adding TMG was dramatic for the case of the α cell. The response at 4.3 kV/cm

increased by a factor of three after the addition of $\approx$2 ppm concentration of TMG. The signal at 13 kV/cm increased so much that it saturated the amplifiers used in the cells (gains were chosen so as to provide maximal signals for running with pure argon). Consequently, the change in response at this collection voltage could not be obtained. This result is consistent with the fact that the α particles travel only a short distance ($\approx$ 40μm) before ranging out in the argon, and deposit all of their kinetic energy ($\approx$ 5.5 MeV) in the immediate region above the source. Recombination of the ionization electrons and argon ions is likely in such regions of intense ionization, and the TMG molecules can therefore help recover some of the lost signal in the manner described above. The addition of the large concentration (100 ppm) nitrogen had an effect similar to the oxygen additions on the alpha signal. However, even this large amount of nitrogen was not sufficient to overcome the opposite effects from the previous addition of TMG.

Turning to Fig. 6.2, we see that, after the introduction of additives, the change in the response of a β cell is markedly different from that observed in an α cell. At the high voltage (10.9 kV/cm), the response of the β cell to small oxygen concentrations is half as large as for the α cell. However, at the low voltage (0.9 KV/cm), the drop in signal for the β cell is greater than for the α cell at any of the two voltages shown in Fig. 6.1 Clearly, the β signal at low voltage is a very sensitive measure of the oxygen content in liquid argon. Within measuring uncertainty, the responses of the β cells are not affected by introduction of 4 ppm nitrogen. The effect of TMG on the β signal is much smaller than on the α sensor. This can be attributed to the fact the βs do not produce as much intense ionization along their paths as do the αs; furthermore, βs are selected for having traversed a minimum of 2.3 mm of liquid argon (see Appendix A), effectively placing an upper limit on the amount of energy deposited through $\frac{dE}{dx}$. The effect of 100 ppm nitrogen on the β cell is roughly the same at both voltages shown.

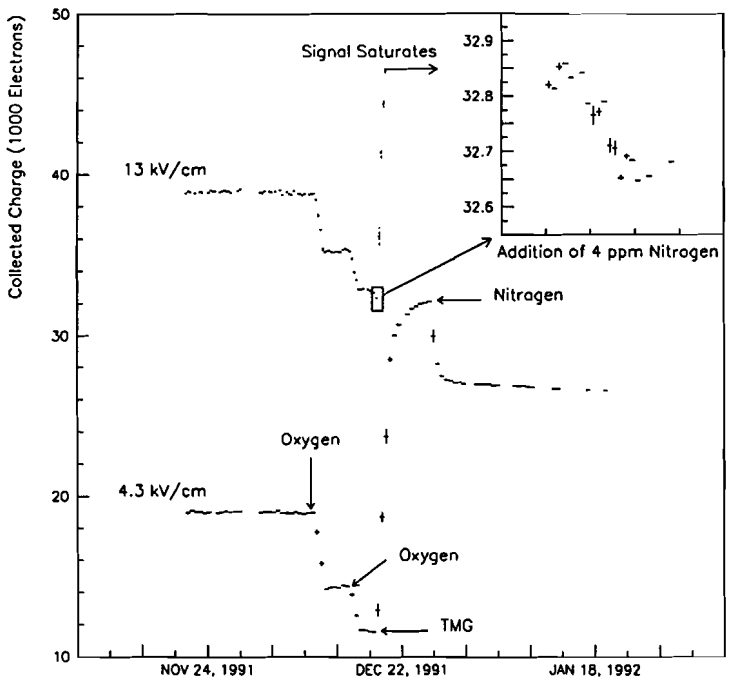

Figure 6.1: History of the signal observed in an α cell as a function of additives mixed into the liquid argon. The response is plotted for charge collection voltages of 13 kV/cm and 4.3 kV/cm. Arrows indicate the introduction of each additive sample. The inset shows the change in response at 13 kV/cm after the addition of $\approx$ 4 ppm of nitrogen.

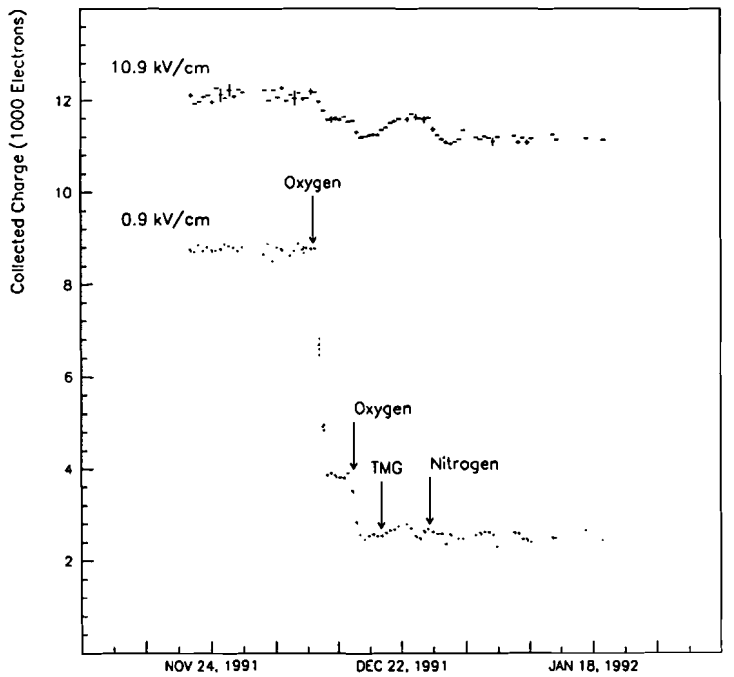

Figure 6.2: Response of a β cell to additives. The signal is plotted versus time for charge collection voltages of 10.9 kV/cm and 0.9 kV/cm. Arrows indicate the introduction of additives.

Table 6.1 summarizes the changes in response of the test cells, after the addition of material to the liquid argon, at several charge-collection voltages. This is given in terms of the size of the signal after each addition, relative to the original signal, namely that prior to the addition of any contaminant.

Table 6.2: Signals observed in test cells after consecutive mixing in of additives to the argon. The responses are given relative to the initial responses of the cells (prior to adding any contaminants).

sensor and electric field	Signals as % of original response				
	1st O_2 sample	2nd O_2 sample	4 ppm N_2	2 ppm TMG	100 ppm N_2
α 4.3 kV/cm	75.62±0.38	61.57±0.49	60.68±0.05	174.1±4.4	145.1±3.4
α 13 kV/cm	90.63±0.15	84.60±0.12	83.72±0.03	N/A	N/A
β 0.9 kV/cm	45.38 ± 0.80	31.1 ± 1.0	30.78 ± 0.91	32.25 ± 0.98	30.5 ± 1.1
β 10.9 kV/cm	95.79 ± 0.08	92.69 ± 0.06	92.88 ± 0.09	96.11 ± 0.12	92.41 ± 0.08

6.2 Response of the Calorimeter to Additives

Since the observed signal in D-Zero calorimeters depends directly on the efficiency of charge collection in the calorimeter cells, any change in this efficiency affects the responses of the calorimeters. The oxygen contamination studies conducted at the test beam will be used to derive corrections to the observed response of each D-Zero calorimeter as a function of the purity of the liquid argon. These corrections will be described in Section 6.4.

Any significant non-linearity in the response of the calorimeter produced through the presence of oxygen in the argon would be of great concern to D-Zero, and would necessarily complicate corrections based on argon purity. Fortunately, no significant energy dependent effect was found, for either electrons or pions, within the energy range of 10 through 150 GeV. Figure 6.3 shows the relative response of the calorimeter to electrons after the addition of the first sample of oxygen. Similar

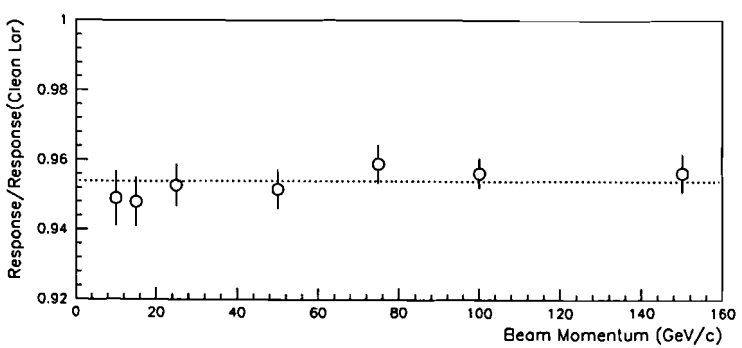

Figure 6.3: Normalized electron response versus energy after the addition of the first sample of oxygen. The electron response at each energy is normalized to the response measured before the addition of the contaminant.

results were obtained for the other additions, and therefore changes in response were averaged across all energies for each given additive.

The results of our studies are summarized in Table 6.3. The observed changes in the response for electrons and for pions are within 1% for each addition of oxygen (the second oxygen data point in Table 6.3 is for after the addition of the 4 ppm of nitrogen into the argon). It is also evident that the additions of TMG and of the 100 ppm nitrogen had very similar effects on electrons and on pions at the normal operating voltage of the calorimeter (10.9 kV/cm). In each case the response of the calorimeter closely tracks the response of the β cells at the same voltage.

Table 6.3: Response of the calorimeter to electrons and pions as a function of additives in the liquid argon. The data are averaged over energies between 10 and 150 GeV.

Response relative to initial signal		
Additive Introduced	Electrons	Pions
1st O_2 sample	95.40% ± 0.22%	94.63% ± 0.41%
2nd O_2 sample[a]	91.92% ± 0.29%	91.33% ± 0.59%
2 ppm TMG	97.75% ± 0.21%	96.47% ± 0.40%
100 ppm N_2	93.56% ± 0.25%	92.27% ± 0.42%

[a] After 4 ppm N_2

6.3 Resolution of the Calorimeter with Additives

It is important to evaluate any possible dependence of the energy resolution of the calorimeter on the purity of the liquid argon. Any significant changes with argon quality would directly affect, for example, measurements of the W particle,

and would require a more extensive Monte Carlo effort to extract the W mass and width from the data. Table 6.4 summarizes the measured energy resolution of the calorimeter before and after the introduction of each additive. The fractional energy resolution was parametrized as:

$$\frac{\sigma}{E} = \left(C^2 + \frac{S^2}{E} + \frac{N^2}{E^2}\right)^{\frac{1}{2}} \tag{6.1}$$

where C, S, and N represent constant (systematic), sampling (statistical), and energy independent (noise) contributions to the resolution, as in Chapter 4. The parameters C, S, and N were fit for electrons. For pions, N was fixed to the measured width of pedestals (noise). Only responses for energies $\geq 10\,\mathrm{GeV}$ were included in these fits.

Table 6.4: Resolution as a function of additives

Electrons			
After sequential addition:	C	S	N
None	0.0005 ± 0.0005	0.137 ± 0.004	0.40 ± 0.01
1 ppm O_2	0.001 ± 0.001	0.137 ± 0.002	0.36 ± 0.03
1 ppm O_2[a]	0.003 ± 0.003	0.136 ± 0.005	0.33 ± 0.03
2 ppm TMG	0.0025 ± 0.0025	0.133 ± 0.012	0.38 ± 0.08
100 ppm N_2	0.003 ± 0.003	0.134 ± 0.009	0.34 ± 0.03
Pions			
None	0.046 ± 0.001	0.485 ± 0.018	1.17
1 ppm O_2	0.038 ± 0.005	0.507 ± 0.027	1.15
1 ppm O_2[a]	0.046 ± 0.007	0.484 ± 0.032	1.11
2 ppm TMG	0.034 ± 0.004	0.510 ± 0.012	1.15
100 ppm N_2	0.040 ± 0.002	0.482 ± 0.016	1.13

[a] With 4 ppm of N_2.

Table 6.4 indicates within errors, the resolution parameters for electrons do not

depend on the presence of additives. A possible exception is the noise (N) term, which appears to decrease, but is nevertheless consistent with the measured width of the pedestals. The value of N represents the effect of the additive on noise from radioactive decays of uranium in the absorber plates. The pion resolutions are also in good agreement, and to do appear to depend on the additives. We consequently do not expect corrections for calorimeter resolution from the presence of small concentrations of impurities in liquid argon.

6.4 Corrections to the Responses of the Calorimeters Using β Cells

We will now discuss the corrections to the response of each D-Zero calorimeter based on the liquid argon purity, as determined from the response of the purity monitors and normalized by test beam data obtained with added oxygen. As shown in Section 6.1, the low voltage response (0.9 kV/cm) of the β cells is highly sensitive to the purity of the liquid argon: typically, about a factor of ten more sensitive than data taken on the high-voltage plateau near 10.9 kV/cm.

Figure 6.4 shows the ratio of the response at 0.9 kV/cm to the response at 10.9 kV/cm for a β cell, as a function of oxygen concentration in the liquid argon. These measurements were performed in a test calorimeter at the University of Rochester [39]. We will use the ratio of low to high voltage responses of the β cells to cross-calibrate the cryostats, because in such ratios systematic effects tend to cancel (e.g., dependence of signal on argon density or temperature, changes in pileup caused by the decay of ^{106}Ru, errors in amplifier calibration, etc). The data

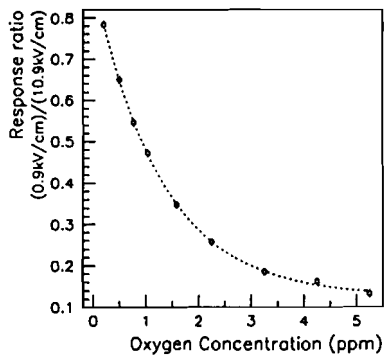

Figure 6.4: The ratio of the response at 0.9 kV/cm to that at 10.9 kV/cm, for a β-type test cell as a function of oxygen contamination [39].

in Fig. 6.4 can be parameterized by the function (see curve in Fig. 6.4):

$$R_\beta(\rho) = Ae^{-B\cdot\rho} + C \tag{6.2}$$

$$A = 0.77 \pm 0.01$$

$$B = 0.78 \pm 0.03$$

$$C = 0.127 \pm 0.008$$

where R_β is the 0.9 kV/cm to 10.9 kV/cm response ratio for the β cell, ρ is the oxygen concentration in the argon in parts per million. A, B, and C, are free parameters determined from by fitting Equation 6.2 to the data. Inverting this relationship gives the oxygen content in the argon as a function of the response ratio.

$$\rho = -\frac{ln(R_\beta - \frac{C}{A})}{B} \tag{6.3}$$

Table 6.5 lists the response ratios for the β cells obtained in the test beam, as well as the expected oxygen concentration calculated using Eq. 6.3.

Table 6.5: β cell response ratios for test beam oxygen studies and estimated oxygen concentrations (ppm)

Additive Introduced	β cell ratio $\frac{0.9\,kV/cm}{10.9\,kV/cm}$	Estimated Oxygen Concentration
None	0.7349 ± 0.0024	0.3008 ± 0.0051
1st O_2 sample	0.3482 ± 0.0064	1.622 ± 0.038
2nd O_2 sample	0.2465 ± 0.0079	2.37 ± 0.11

Using the calorimeter results given in Table 6.5, the response of any D-Zero calorimeter can now be normalized to the 1991 test-beam response. Fitting a second order polynomial through the three data points in Table 6.5 as a function of oxygen concentration (averaging pion and electron responses), yields the following result:

$$R_C = P_0 + P_1 \cdot \rho + P_2 \cdot \rho^2 \tag{6.4}$$

$$P_0 = 1.0096 \pm 0.0033$$

$$P_1 = -0.030 \pm 0.013$$

$$P_2 = -0.0038 \pm 0.0034$$

where R_C is the response ratio of the calorimeter as a function of oxygen concentration in the argon, normalized to the value of the response ratio obtained in the test beam calorimeter before the introduction of oxygen (i.e., normalized to

$\rho = .30$). Equation 6.4 was applied to the data from the β cells contained in the D-Zero calorimeters, and the results are summarized in Table 6.6 (Also included is the 1990 test beam measurement.)

Table 6.6: Response of D-Zero calorimeters relative to 1991 test beam.

Cryostat[a]	Response Ratio for β Cells	Estimated Oxygen Concentration (ppm)	Correction to Signal (relative to 1991 TB)
1990 TB	0.7584 ± 0.0045	0.252 ± 0.011	$99.83 \pm 0.47\%$
CC	0.7497 ± 0.0039	0.270 ± 0.008	$99.89 \pm 0.49\%$
ECN	0.7405 ± 0.0065	0.289 ± 0.014	$99.95 \pm 0.51\%$
ECS	0.7400 ± 0.0092	0.290 ± 0.019	$99.95 \pm 0.51\%$

[a]Test Beam, Central Calorimeter, End Calorimeter North, End Calorimeter South

6.5 Correcting response Using α Cells

A similar correction method may be implemented using response ratios from the α cells. However, the dependence of the α response on charge collection voltage is less sensitive to oxygen concentration than the form of the β response. Consequently, the method of ratios is expected to be far less sensitive when applied to the data from the α cells. Nevertheless, several advantages to using α sources can be exploited in comparing the response of different cells at 13 kV/cm. Because signals from α sources are bigger and narrower than for β signals, they provide a higher signal to noise ratio. Also α sources do not have large rate dependent effects; that is, the long half-life ($\approx$400 years) of ^{241}Am made it possible to select weaker sources that would not degrade markedly over the lifetime of D-Zero. Finally, α signals show very little sensitivity to the density of the liquid argon, and the absolute signals at 13 kV/cm are about twice as sensitive to oxygen concentration as the β signals on the high-voltage plateau.

When directly comparing test cell signals several calibration factors must be taken into account. For example, variations in amplifier gains, charge-sharing between the detector and amplifiers (e.g., detector capacitance), variations in coherent noise, and other subtleties, effects which would tend to cancel in ratios of responses, can affect the absolute comparisons. A particular problem in such comparisons of data from different cryostats is the effect of nitrogen (and other contaminants besides oxygen) on the response of α cells. A few ppm of nitrogen can suppress α signals by about one percent, but will have essentially no effect on the response of calorimeters or of β cells.

The absolute signals of all D-Zero and test beam calorimeters agree in their α responses to within about 3%. Assuming oxygen as the cause for any differences, this sets an upper limit of 1.7% on difference in response among the calorimeters. This is clearly inconsistent with the results obtained using β cells. A 3% difference in α response could be caused by small amounts of nitrogen alone, which would correspond differences on the order of 0.5% in response among the calorimeters. This is essentially consistent with the β measurements, however, due to the systematic uncertainties discussed above, this number may only be interpreted as an approximate limit.

Clearly, the absolute response of α cells is at present not a sufficiently strong tool for cross-calibration of calorimeters. The signal losses observed for all α cells, at a field of 13 kV/cm, throughout the 1992-3 collider run at D-Zero, corresponded to less that 0.01% per year [40], indicating exceptional stability of the argon purity throughout the run. Consequently, it would appear that the α sources best suited for measuring time dependence of relative argon quality in a single cryostat.

6.6 Summary

Addition of oxygen to the liquid argon has no significant effect on the linearity or energy resolution of calorimeters. A simple scale correction should therefore suffice for correcting the energy response of a given D-Zero calorimeter for any oxygen contamination. The method we propose for correcting D-Zero calorimeter responses based on data from β cells has sensitivity at the 0.5% level. The β cells indicate a variation of response due to effective oxygen contamination of less that 0.2%. The anticipated correction throughout any D-Zero run will be of the order of a few percent. At present, the α cells cannot be used for cross-calibrating calorimeters, although they offer excellent sensitivity to relative changes in argon quality over the course of a data run. In the following chapter we consider the response of the test beam calorimeter to variations in the charge collection voltage.

Chapter 7

High Voltage Dependence of Calorimeter Response and Ionization Content of Particle Showers

The dependence of the D-Zero central calorimeter on the charge collection voltage was evaluated during the 1991 test-beam run. The high voltage response of the calorimeter to electrons and pions at energies of 5, 10, and 100 GeV was measured prior to conducting the additive studies, which were discussed in the previous chapter. After the introduction of each additive, similar data were taken for 10 and 100 GeV electrons and pions, and the analysis of those data will be presented in this chapter.

7.1 High Voltage Response with Clean Argon and with Added Oxygen

The high voltage response of the calorimeter is qualitatively similar to the response observed for a β ionization cell (Appendix A) – essentially that for a minimum ionizing particle. The high voltage response to a heavily ionizing particle is typified by the response of an α ionization cell (Appendix A). Any particle that produces ionization that is subject to significant recombination loss may be considered a heavily ionizing particle. This can be a low velocity particle, such as an electron or more massive hadron, or a nuclear fragment. Barring the presence of contaminants in the argon, the signal for minimum ionizing particles rises rapidly with voltage and saturates (plateaus) at some maximum value. For hadronic showers, in particular pion showers, which can contain many heavily ionizing particles [41], the response might be expected to rise more slowly with voltage.

The high voltage response for both α and β cells are shown in Fig. 7.1. The curves are obtained from fits to all the test-beam α and β monitors, using data taken before the introduction of any additives to the calorimeter. The β data were fit to the expression:

$$Q_b(\mathcal{E}) = Q_0 \cdot L/D \cdot (1 - L/D \cdot (1 - e^{-D/L})) \tag{7.1}$$

which describes the collection of total charge Q_0, that is evenly deposited across the argon gap (D), subject to no recombination loss. $L = A\mathcal{E} + B$ is the attenuation of the free electrons as a function of electric field $\mathcal{E}$. We have generalized a standard form for the attenuation length, which is linear in the electric field, to include a constant term [36]. The α data were fit to a simple second order polynomial:

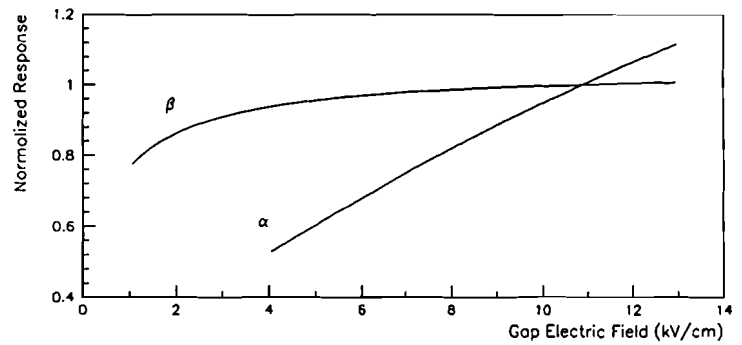

Figure 7.1: α and β ionization cell responses as a function of charge collection electric field. Responses from individual cells were rescaled to the mean value at 10.9 kV/cm.

$$Q_a(\mathcal{E}) = C_0 + C_1 \cdot \mathcal{E} + C_2 \cdot \mathcal{E}^2 \tag{7.2}$$

Using a simple model, the high voltage response of the calorimeter can be described by assuming that the ionization is due to a combination of heavily and minimum ionizing components [42]. If all the ionizing particles traversing the gaps were minimum ionizing, then the plateaus could be described by a properly normalized β cell plateau, namely $C_m \cdot Q_b(\mathcal{E})$, where C_m is a scale constant. However, if the particles were all heavily ionizing, with energy deposition similar to α particles, then the plateaus could be described by $C_h \cdot Q_a(\mathcal{E})$. For a shower that has both types of particles in the gap, we can write

$$Q_s(\mathcal{E}) = C_m \cdot Q_b(\mathcal{E}) + C_h \cdot Q_a(\mathcal{E}) \tag{7.3}$$

where C_m and C_h would, in general, be expected to depend on the energy of an incident particle.

Assuming that $Q_b(\mathcal{E})$ can be used to represent only minimum ionizing particles, the expression for $Q_s(\mathcal{E})$ was fit to the normalized high-voltage response for electron and pion showers, for voltage scans taken with clean argon, and after the two additions of oxygen. That is, each excitation function was fit to a linear combination of the two responses from the test cells. We chose to normalize the α and β response shapes to unity at the nominal value of operating field (10.9 kV/cm). Small variations exist in the fields within the argon gaps of the uranium calorimeter modules due to the accumulation of charge on the surfaces of the uranium absorber plates (actually on the external uranium oxide) [43]; the uncertainty in the field caused by this effect was estimated to be ≈0.1-0.4 kV/cm. Since the response is not very sensitive to the field at voltages on the plateau, only data above 4.3 kV/cm were used in the fits so as to minimize any bias.

Figure 7.2 shows the fit to the 100 GeV pion data with and without a heavily ionizing (α) component. Clearly, a heavily ionizing component is required to describe the data. Fits to electron as well as pion data for clean argon at 100 GeV (again, data normalized at the operating voltage) are shown in Fig. 7.3. The results for all fits to the data taken with clean argon are summarized in Table 7.1. Columns 3 and 4 list the estimated fractions of heavily (α cell) and minimum (β cell) ionizing components of electron and pion showers at various energies (uncertainties are given in parentheses). For the values in columns 5 and 6, we used an ad hoc correction that was applied to the calorimeter response based on the known voltage settings. The correction assumed an offset voltage of -0.33 kV/cm in the uranium modules due to accumulated surface charges, and its magnitude was derived from the dependence of the response on voltage. The correction for pions was slightly smaller than for electrons, because part of their energy is deposited in the

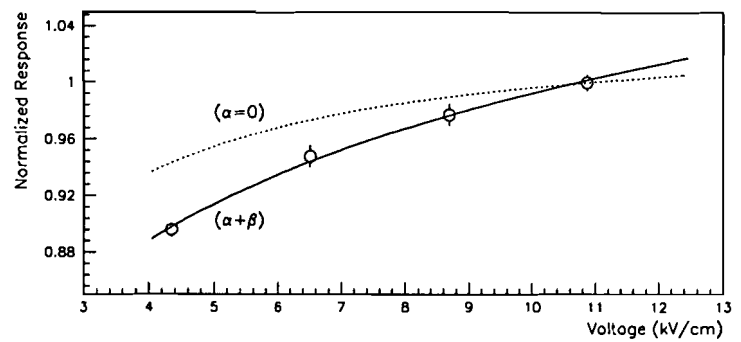

Figure 7.2: Fits to 100 GeV/c pion response with and without a heavily ionizing component.

Table 7.1: Fitted shower components for electron and pion responses in clean argon.

		No Field Correction		With Field Correction	
Particle	E(GeV)	C_m	C_h	C_m	C_h
Electron	5	0.922(.011)	0.079(.013)	0.935(.011)	0.069(.012)
Electron	10	0.936(.011)	0.065(.012)	0.949(.008)	0.051(.009)
Electron	100	0.955(.004)	0.046(.005)	0.965(.004)	0.037(.005)
Pion	5	0.840(.030)	0.154(.036)	0.856(.034)	0.141(.037)
Pion	10	0.847(.026)	0.136(.030)	0.855(.022)	0.133(.025)
Pion	100	0.881(.011)	0.121(.013)	0.894(.012)	0.110(.014)

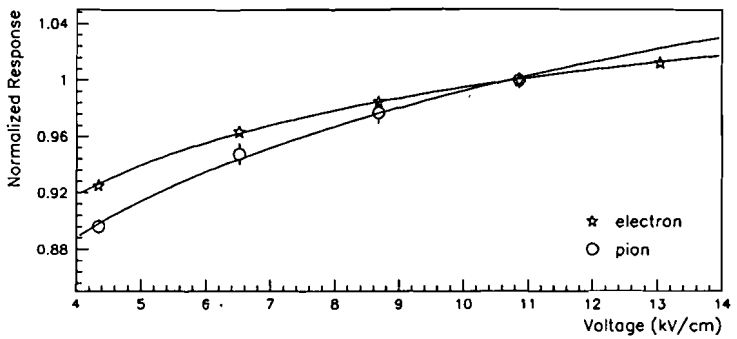

Figure 7.3: Voltage dependence of response for 100 GeV electrons and pions.

coarse hadronic (CH) modules, which use copper absorber plates, and therefore are unaffected by the buildup of surface charge. (On average, 15% of the energy from a 100 GeV pion shower is deposited in CH modules. This fraction reduces to 10% for 10 GeV pions.) Clearly, such corrections can only serve as crude approximations since we have no accurate measure of the surface charge densities, moreover these charges are likely to vary from cell to cell in the calorimeter. However, it is worth noting that corrections of this type do not qualitatively affect the results of the fits shown in Table 7.1. C_h, the estimated fraction of heavily ionizing particles for showers, clearly tends to be larger for pions than for electrons.

Similar fits were performed on the data after each addition of oxygen to the calorimeter, these results are summarized in Table 7.2. We expect the heavily and minimum ionizing components of the deposited charge to remain constant throughout the introductions of additives to the argon. However, systematic differences in the surface charges on the uranium plates among the data sets prevents such a comparison. Such fits were not possible after the addition of TMG, because of the

Table 7.2: Fitted shower components for electron and pion responses after addition of oxygen.

	After Addition of ≈ 1 ppm Oxygen				
		No Field Correction		With Field Correction	
Particle	E(GeV)	C_m	C_h	C_m	C_h
Electron	10	0.952(.010)	0.043(.010)	0.977(.006)	0.022(.006)
Electron	100	0.949(.004)	0.045(.004)	0.973(.004)	0.025(.004)
Pion	10	0.891(.033)	0.099(.036)	0.916(.022)	0.079(.022)
Pion	100	0.906(.011)	0.087(.011)	0.928(.008)	0.069(.008)
	After Total ≈ 2 ppm Oxygen+ 4 ppm Nitrogen Added				
Electron	10	0.896(.005)	0.096(.005)	0.939(.006)	0.056(.007)
Electron	100	0.899(.005)	0.091(.005)	0.943(.008)	0.051(.008)
Pion	10	0.836(.030)	0.152(.035)	0.875(.031)	0.117(.036)
Pion	100	0.878(.008)	0.112(.008)	0.913(.009)	0.080(.009)

saturation of the α signal at relatively low collection voltages.

7.2 High Voltage Dependence of $\frac{e}{\pi}$ Response

The dependence of the relative response of the calorimeter to electrons and pions (the "$\frac{e}{\pi}$ ratio") as a function of the collection voltage also suggests that electron and pion showers have different ionizing components that are affected differently by variations in field strength. The $\frac{e}{\pi}$ response ratios for clean argon at 10 and 100 GeV are shown at the top of Fig. 7.4; both data sets are normalized to unity at 10.9 kV/cm. Also shown are the $\frac{e}{\pi}$ ratios as a function of voltage after the first and second addition of oxygen. (Again, the 4 ppm of nitrogen was included with the second oxygen addition.) The $\frac{e}{\pi}$ ratio decreases with increasing field for clean argon. With the addition of oxygen to the calorimeter, this dependence appears to be lessened. While the $\frac{e}{\pi}$ ratio at the operating voltage was consistent with the value for clean argon, the ratio is nearly independent of field, as shown in Fig. 7.4. (All data are normalized to the measured $\frac{e}{\pi}$ ratio for clean argon at 10.9 kV/cm.)

The difference observed in Fig. 7.4 between the data sets with added oxygen and the original argon may again be due to the fact that pions deposit a portion of their energy in CH modules. Since the response of the calorimeter as a function of voltage is much steeper between 2 and 4.3 kV/cm for oxygen doped argon than for pure argon (See tables in Section 7.3.), the pion signal may be receiving a significant enhancement from the higher field values in the CH modules (without uranium).

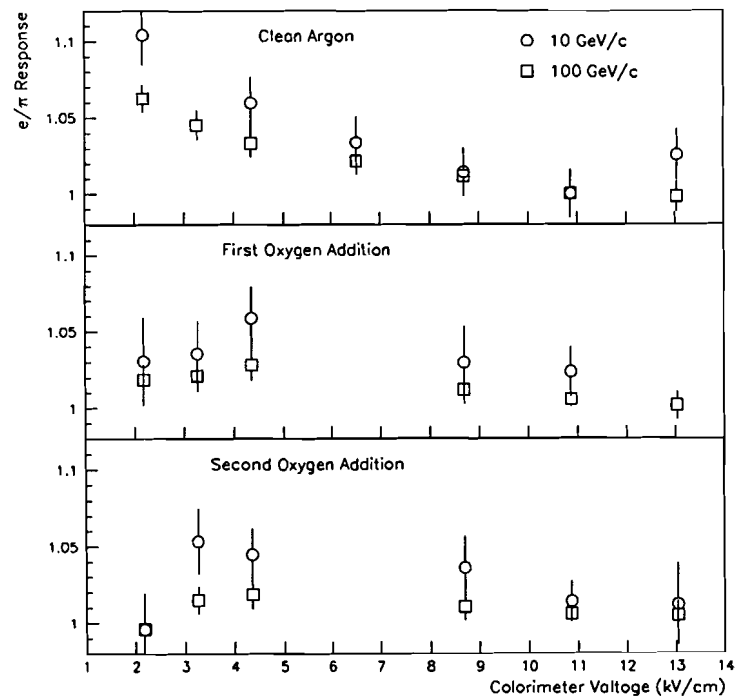

Figure 7.4: The $\frac{e}{\pi}$ response as a function of electric field for 10 and 100 GeV. Data are shown for three concentrations of oxygen in the liquid argon. From top to bottom the oxygen concentrations are approximately 0.3,1.6,2.4 ppm respectively. All data are normalized to the measured $\frac{e}{\pi}$ ratio for clean argon at 10.9 kV/cm.

7.3 Summary of High Voltage Scan Data

This section contains a summary of the high voltage scans of the calorimeter. The data are provided for completeness and for any further application. All responses are given in GeV and errors are listed in parentheses.

Table 7.3: Calorimeter high voltage response for clean argon – 10 GeV

Voltage	Electron Response	Pion Response
500	8.030(0.053)	7.114(0.116)
750		
1000	8.976(0.055)	8.288(0.123)
1500	9.349(0.061)	8.849(0.134)
2000	9.592(0.062)	9.252(0.133)
2500	9.789(0.058)	9.577(0.140)
3000	9.882(0.062)	9.426(0.141)
3800		

Table 7.4: Calorimeter high voltage response after first oxygen addition – 10 GeV

Voltage	Electron Response	Pion Response
500	4.825(0.036)	4.580(0.123)
750	6.440(0.031)	6.084(0.122)
1000	7.426(0.043)	6.862(0.129)
1500		
2000	8.854(0.057)	8.415(0.190)
2500	9.157(0.054)	8.752(0.128)
3000	9.410(0.040)	
3800	9.579(0.062)	9.189(0.211)

Table 7.5: Calorimeter high voltage response after second oxygen and 4 ppm nitrogen addition – 10 GeV

Voltage	Electron Response	Pion Response
500	3.543(0.021)	3.481(0.081)
750	5.231(0.029)	4.859(0.093)
1000	6.411(0.032)	6.003(0.093)
1500		
2000	8.472(0.048)	8.000(0.153)
2500	8.838(0.035)	8.525(0.105)
3000	9.113(0.057)	8.807(0.225)
3800		

Table 7.6: Calorimeter high voltage response after TMG addition – 10 GeV

Voltage	Electron Response	Pion Response
500	3.650(0.020)	3.452(0.076)
750	5.388(0.028)	5.193(0.088)
1000	6.630(0.026)	6.415(0.088)
1500		
2000	9.026(0.053)	8.487(0.113)
2500	9.421(0.049)	9.028(0.133)
3000	9.736(0.057)	9.332(0.176)
3800	10.048(0.060)	9.784(0.181)

Table 7.7: Calorimeter high voltage response after 100 ppm nitrogen addition – 10 GeV

Voltage	Electron Response	Pion Response
500	3.584(0.020)	3.469(0.083)
750	5.256(0.030)	5.020(0.091)
1000	6.401(0.036)	6.133(0.111)
1500		
2000	8.479(0.052)	8.324(0.180)
2500	8.920(0.033)	8.696(0.065)
3000	9.258(0.057)	8.655(0.183)
3800		

Table 7.8: Calorimeter high voltage response for clean argon – 100 GeV

Voltage	Electron Response	Pion Response
500	81.594(0.333)	77.580(0.622)
750		
1000	90.683(0.256)	89.010(0.496)
1500	94.421(0.382)	94.123(0.750)
2000	96.520(0.387)	97.030(0.769)
2500	98.001(0.276)	99.331(0.548)
3000	99.235(0.398)	
3800		

Table 7.9: Calorimeter high voltage response after first oxygen addition – 100 GeV

Voltage	Electron Response	Pion Response
500	49.534(0.203)	49.111(0.430)
750	65.563(0.262)	64.859(0.591)
1000	75.265(0.321)	73.927(0.659)
1500		
2000	90.400(0.351)	90.251(0.727)
2500	93.303(0.184)	93.702(0.410)
3000	95.493(0.381)	96.298(0.801)
3800	97.677(0.394)	98.664(0.823)

Table 7.10: Calorimeter high voltage response after second oxygen and 4 ppm nitrogen addition – 100 GeV

Voltage	Electron Response	Pion Response
500	36.032(0.144)	36.535(0.311)
750	53.333(0.212)	53.068(0.435)
1000	65.197(0.256)	64.632(0.521)
1500		
2000	85.540(0.338)	85.479(0.674)
2500	89.669(0.206)	90.015(0.406)
3000	92.249(0.373)	92.702(0.798)
3800		

Table 7.11: Calorimeter high voltage response after TMG addition – 100 GeV

Voltage	Electron Response	Pion Response
500	37.201(0.144)	38.013(0.304)
750		
1000	67.388(0.267)	
1500		
2000	91.810(0.363)	90.436(0.708)
2500	95.882(0.259)	95.667(0.357)
3000	98.639(0.390)	98.415(0.763)
3800	102.472(0.296)	102.455(0.799)

Table 7.12: Calorimeter high voltage response after 100 ppm nitrogen addition – 100 GeV

Voltage	Electron Response	Pion Response
500	36.850(0.148)	
750	53.988(0.214)	53.877(0.516)
1000	65.665(0.254)	
1500		
2000	86.337(0.342)	86.112(0.674)
2500	91.304(0.250)	91.283(0.361)
3000	94.411(0.371)	94.384(0.738)
3800		

Table 7.13: Calorimeter high voltage response for clean argon – 5 GeV

Voltage	Electron Response	Pion Response
500	3.812(0.030)	3.170(0.071)
750	4.219(0.034)	3.493(0.109)
1000	4.374(0.037)	3.726(0.077)
1500	4.612(0.034)	3.995(0.093)
2000	4.725(0.034)	4.248(0.097)
2500	4.821(0.040)	4.313(0.111)
3000	4.899(0.036)	4.395(0.097)
3800		4.461(0.106)

Chapter 8

Conclusions

The data and analyses presented in this dissertation provide information concerning calibration issues for the D-Zero calorimeters and offer a qualitative measure of the character of ionization produced in electron and pion showers. Such data are essential for understanding the physics signals to be studied at the collider.

8.1 Low-Energy Response of the Calorimeter and the Jet Energy Scale

The response of the D-Zero central calorimeter was found to be linear to within 1% accuracy for electrons in the energy range between 4 and 150 GeV and the response for pions was linear to within 2% accuracy for energies down to 10 GeV. Any non-linearities at low energy can produce non-linearities in the response of the calorimeter to jets, and therefore errors in measurement of the jet energy. The calculations discussed in Chapter 5 predict 4% uncertainties in the corrections for jet energies of 200 GeV which become about 8% for 25 GeV jets [29]. The data and selections presented here have been used to create a "particle shower library"

containing the cell by cell energy depositions of particles, which will be used for more detailed simulations of the calorimeter's response to jets as part of a future thesis [19].

8.2 Response Corrections

The response of the D-Zero calorimeters was calibrated to the response of the argon purity monitors. This offers a method for cross-calibration of each calorimeter to within $\approx$0.5% accuracy for the expected level of oxygen concentrations. Studies of the response of the central calorimeter with added oxygen show that oxygen suppresses the response by about 3%/*ppm* of oxygen concentration. Further, this suppression of signal at the calorimeter's operating voltage, is essentially constant across a large energy range for both pions and electrons, and the energy resolutions are consistent with those obtained using clean argon.

8.3 Calorimeter High Voltage Scans and Characteristics of Ionization for Electron and Pion Showers

The high-voltage response of the calorimeter for electrons and pions suggests that pion showers have components that ionize the argon more intensely than in the case of electron showers. Much research has been performed to study the effect of adding photo-sensitive dopants to liquid argon, and especially of the effect on the observed signals from heavily ionizing particles (see, for example [37, 44, 45]). The aim of these efforts has, in part, been to provide a mechanism for improving the compensation of liquid nobel gas calorimeters by converting photons produced in

electron-ion recombination into observable signals. The addition of a 2 ppm concentration of TMG had no significant effect on the $\frac{e}{\pi}$ ratio of our calorimeter. This is most likely due to the relatively small excess of heavy ionization in pion showers as suggested by the simple model we introduced in Chapter 7. Higher concentrations of TMG may produce a larger effect, however, allowable concentrations are severely limited by the solubility limits of the photo-sensitive dopants [37]. Because the pion signal rises faster with high voltage than the electron signal, higher operating voltages may effect compensation, however, such adjustments will not suffice for achieving equalization of electron and pion response, and are highly sensitive to oxygen concentrations. We conclude that, at present, there is no simple mechanism for improving the $\frac{e}{\pi}$ response of liquid-argon calorimeters.

Bibliography

[1] F. Dydak, Proceedings of the XXV International Conference on High Energy Physics, Singapore (1990).

[2] A. Clark, *Experimental Aspects of Hadron Collider Physics*, Techniques and Concepts of High Energy Physics VI, edited by T. Ferbel, (Plenum Press, 1991) 71.

[3] *Testing the Standard Model*, Proceedings of the 1990 Theoretical Advanced Study Institute in Elementary Particle Physics, Ed. M. Cvetič and P. Langacher, (World Scientific, 1991).

[4] Abe F., et al., *Lower Limit on the Top-Quark Mass from Events with Two Leptons in* $p\bar{p}$ *Collisions at* $\sqrt{s} = 1.8$ *TeV*, Phys. Rev. Let., **68**, 447 (1992).

[5] D-Zero Collaboration, *The DØ Detector*, submitted to NIM.

[6] A. Zylberstein, *The Transition Radiation Detector for the D-Zero Experiment*, Proceedings of the 7th Annual Conference on Proton-Antiproton Physics, Fermilab (1988).

[7] Denisov, *Small Angle Muon System (SAMUS) for the D0 Detector at Fermilab*, General Collaboration Meeting, D0Note #1376, February 1992.

[8] Wigmans, R., *Nucl. Instrum. Methods* A259: 389 (1987)

[9] Wigmans, R., *Advances in Hadron Calorimetry*, Annu. Rev. Nucl. Part. Sci. 1991. 41:133-85.

[10] Storm, E., Israel, H. I., *Nucl. Data Tables* 7: 565 (1970).

[11] Pages, L., et al. *Atomic Data* 4: 1 (1972).

[12] U. Fano, Ann. Rev. Nucl. Sci. **13**, 1 (1963).

[13] Fabjan, C. W., Wigmans, R., *Energy Measurement of Elementary Particles*, Reports on Progress in Physics, 52:1519 (1989).

[14] B. Cox, *Uranium - Liquid Argon Calorimetry: Preliminary Results from the D0 Tests*, Presented at the DPF Meeting of the American Physical Society, Eugene, Oregon, Aug 12-15, 1985.

[15] M. Abolins, et al., *Hadron and Electron Response of Uranium/Liquid Argon Calorimeter Modules for the DØ Detector*, NIM, **A280:36** (1989).

[16] S. Abachi et al., *Beam Tests of the D-Zero Uranium Liquid Argon End Calorimeters*, NIM, **A324:53** (1993).

[17] De, K., *Test Beam Studies of the D0 Calorimeter with 2-150 GeV Beams.*, Proceedings of the XXVI International Conference on High Energy Physics, Aug. 6-12, 1992.

[18] Geld T., PhD Thesis, University of Michigan, 1993.

[19] Borders J., PhD Thesis, University of Rochester, 1993.

[20] Bartlett J. F, et al., *The EPICS System: an Overview*, Fermilab-TM-1244-fiche (1984).

[21] R. Lipton et al., "1990 Test Beam Performance and Studies", D0 Note #1076, January 1991.

[22] M. Tartaglia, "Measurement of the D0test Beamline using Cherenkov Pressure Curves", Note #1660, March 1993.

[23] D. Owen, Private Correspondence

[24] *CRC Handbook of Chemistry and Physics*, ed. David R. Lide, (CRC Press, 1991).

[25] Geant 3.14, R. Brun, et al., CERN.

[26] W. Chen, "Plate Monte Carlo (v3.124) Comparison with Pion Data", D0 Note #1626, December 1993.

[27] Low Energy Monte Carlo calculations courtesy of Wei Chen.

[28] D. Kewley, G. Blazey, J. Chiu, T.Ferbel, *Improving Energy Resolution of Calorimeters Using a Covariance Matrix Approach*, Nucl. Instr. Meth. A280:36, 1989.

[29] Milder A., Astur R., "Jet Energy Scale using Test Beam Data", D0note #1595.

[30] J. Huth, "Jet Energy Measurement: CDF Experience", Proceedings of the SSC Calorimetry Workshop, Tuscaloosa, Al 1989.

[31] Astur R., *A Study of the Ability of the D0 Detector to Measure the Single Jet Inclusive Cross Section*, PhD Thesis Michigan State University, 1992.

[32] F. Abe, et at., "Inclusive Jet Cross Section in $p\bar{p}$ Collisions at $\sqrt{s} = 1.8\,\mathrm{TeV}$", Physical Review Letters, *68* (1992), 1104.

[33] Sjostrand, T., *PYTHIA 5.6 AND JETSET 7.3: PHYSICS AND MANUAL*, CERN-TH-6488-92, May 1992.

[34] Marchesini G., et al., *HERWIG: A Monte Carlo Event Generator For Simulating Hadron Emission Reactions With Interfering Gluons. Version 5.1*, Comput. Phys. Commun. 67 (1992) 465-508.

[35] Paige, et al., *ISAJET 5.30: A Monte Carlo Event Generator For P P and Anti-P P Interactions*, Published in Snowmass Summer Study 1986:320.

[36] W. Hofmann et al., Nucl. Instr. and Meth. 135, (1976) 151.

[37] D.F. Anderson, N.A. Amos, *Prospects for using photosensitive dopants to improve the e/π ratio of liquid argon calorimeters*, Nucl. Instr. and Meth. A309, (1991) 69-76.

[38] Sakai Y., et al., *Drift velocity and life-time of excess electrons in liquid N_2/Ar mixtures*, Proc. of International Conference on Liquid Radiation Detectors, Tokyo (1992).

[39] Data courtesy of G. Blazey, T. Budka, E. Pitts

[40] G. Blazey, Personal Corresponsdence

[41] Brau J., Furuno, K., *Hadron Calorimetery - Optimizing Performance*, Proceedings of the 1st International Conf. on Calorimetry in High Energy Physics, Fermilab, Batavia, Il., 29 Oct. - 1 Nov., 1990.

[42] Blazey G., Hirosky R., *The Minimum and Heavily Ionizing Components of Particle Showers*, Proc. of International Conference on Liquid Radiation Detectors, Tokyo (1992).

[43] McCarthy, R. L., Malter Theory of DC Currents in Uranium Modules, D0Note #780, November 1988.

[44] Shibamura, E., *Energy resolution in liquid Ar or Xe ionization chamber doped with photo-ionizing molecules*, Proc. of International Conference on Liquid Radiation Detectors, Tokyo (1992).

[45] Vuillemin V., et al., *Electron Drift Velocity and Characteristics of Ionization of Alpha and Beta Particles in Liquid Argon Doped with Ethylene for LHC Calorimetry*, Nucl. Instrum. Methods, A316 (1992).

[46] Radeka V., et al., *Semiconductor Detectors and Readout Electronics: Present Directions and Outstanding Problems*, Nucl. Instrum. Methods A253 (1987) 309-312.

[47] Blazey G., et al., Work in Progress.

[48] Goodwin R., et al., *The Proposed Monitoring System for the Fermilab D0 Colliding Beams Detector*, Nucl. Instrum. Methods, A247 (1986).

[49] D0note #745, The Computer Controlled VME High Voltage System for the D0 Detector, D0 Collaboration (presented by S. Wimpenny at the International Conference on Advanced Technology and Particle Physics, Como, Italy, June 13-17, 1988), 8/1/88

Appendix A

The D-Zero Liquid Argon Purity Monitors

The observed signal of the D-Zero calorimeters depends directly on the efficiency with which liberated charge (in the form of ionization electrons) is collected in the liquid argon (LAr) layers. Any electronegative contaminant present in the LAr can combine with the free electrons and reduce this collection efficiency. Thus, a precise measure of the quality of the LAr is essential in order to examine the purity of initial LAr deliveries, in order to transfer calibration data from the D-Zero Test Beam to the D-Zero detector in order to minimize systematic differences in response among the three D-Zero calorimeters, and to verify the stability of response over the course of a data run. This appendix describes the LAr Purity Monitoring system used in the D-Zero experiment.

The D-Zero liquid argon monitoring system utilizes various sensors that measure how well LAr transports ionization. There are six channels instrumented in each of the three D-Zero cryostats, eight in the D-Zero test beam cryostat, and two channels in each of the external test stations. Multiple channels are used to

monitor any variations of LAr purity within a single volume. Each volume contains two types of sensors, namely "α" and "β"cells.

A.1 Sensors

An α sensor has two conducting planes with an electro-deposited α emitter embedded onto one of the planes. A charge-sensitive preamplifier is connected to this source (or sense) plane and a high voltage supply to the second (anode) plane. Figure A.1 illustrates the sensor geometry.

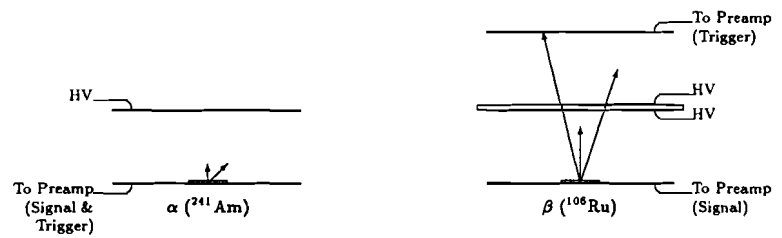

Figure A.1: α and β sensor configurations

Emitted α particles ionize the LAr in the gap between the planes. By placing a positive high voltage on the second plane, the freed electrons can be induced to drift across the gap. The amplifier detects the resultant current, which is linearly dependent on the α particle's energy, and approximately linearly dependent on voltage (and presence of impurities) [36].

The heavily ionizing α particles deposit all of their energy within $\approx 40\mu m$ of the sense plane. Most of the liberated electrons recombine readily with the argon ions in this region of dense ionization and fail to drift to the anode; however, increased

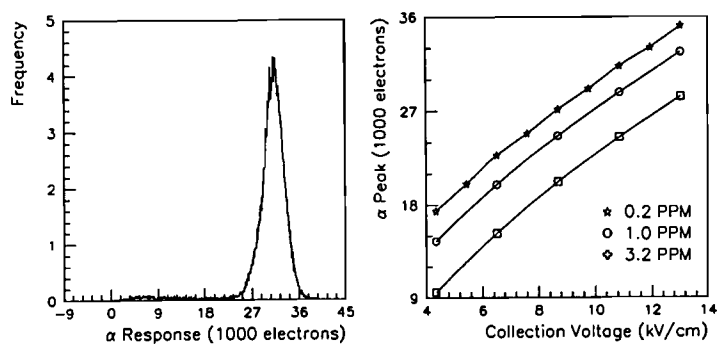

Figure A.2: α spectrum and response versus field for different oxygen contaminations

voltage can accelerate more electrons away from the recombinant centers. Because electrons that escape recombination with the ionized LAr atoms drift across the entire argon gap, any capture by electronegative contaminants decreases the observed signal and provides excellent sensitivity to the presence of such impurities. The α sensors utilize ^{241}Am sources of $\approx 0.05\mu$Ci (half-life of $\approx$400 years, and nearly a monoenergetic spectrum of 5.5 MeV). In LAr, this source provides an initial charge deposition of about 10^5 electrons (of which about 3.1×10^4 are collected at 10.9 kV/cm in clean LAr). Figure A.2 shows the signal spectrum for an imposed collection voltage of 10.9 kV/cm, and the sensor response as a function of voltage for several levels of oxygen concentration. The small excess at signals below the peak in the pulse height distribution is caused by α particles that lose part of their energy in the source material before entering the argon and spurious triggers on noise. [36].

The α sensor provides the response to heavily ionizing particles. Also, the fact that the output is based on one electronic signal at the trigger stage may result in

a bias towards small signals with positive noise fluctuations. For these reasons, α signals are useful only at charge collection voltages in excess of 4.3 kV/cm.

The β sensor, also shown in Figure A.1, uses an electron emitter and thereby provides a signal for a different species of particles. In a β cell, the α source is replaced with a β source, and a second high voltage gap is added to the sensor. If a β particle is emitted with sufficient energy ($\gtrsim$ 2 MeV), it may traverse both gaps, leaving a trail of ions and electrons. The signal in the second gap can be amplified and used as a trigger for the signal in the first gap, which corresponds essentially to a minimum ionizing particle (MIP).

By definition, MIPs deposit little charge when traversing matter, only $\approx 10^4$ electrons in a 2.3 mm of gap LAr and the requirement on a β particle to reach the second gap effectively limits the $\frac{dE}{dx}$ loss of each β that causes a trigger. The difficulties inherent in precisely measuring such small signals can be overcome partially by taking advantage of the fast turn-on of the β sensor's response with HV. At low fields ($\lesssim$ 1.0 kV/cm), a large fraction of the ionization electrons can recombine with argon ions along the electron's path, however as the field is increased, the collection efficiency quickly approaches 100%. For reasonably clean argon ($\lesssim$ 0.5 ppm O_2), the collection efficiency is about 75% at 0.9 kV/cm and nearly 100% above 6.5 kV/cm. Keeping the trigger gap at 10.9kV/cm provides a constant and maximum trigger signal (for a given oxygen concentration). The sensors use $0.05 - 0.5\mu$Ci ^{106}Ru sources (half-life of $\approx$1 year and an endpoint energy of 3.5 MeV). Figure A.3 shows the β signal for an imposed charge collection voltage of 10.9 kV/cm, and the response as a function of voltage for several concentrations of oxygen. The shape of the signal distribution reflects the difference in path lengths of the β particles through the LAr gap, as well as the energy distribution of the emitted β particles, signal spread due to electronic noise, and the pileup of signal from the βs emitted close in time (relative to the time for signal shaping) [46].

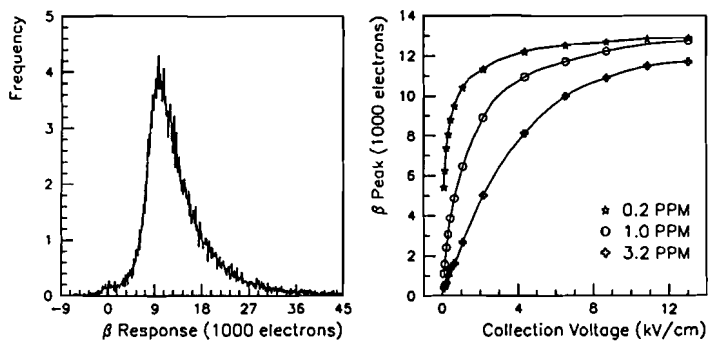

Figure A.3: β spectrum and response versus field for different oxygen contaminations

Only about 12% of the β particles emitted produce a signal in the trigger gap. The remaining particles deposit energy in the first gap which can produce background to the signals that have triggers. The probability of sensitivity to such background, clearly, depends on the activity of the β source (as well as on integration time for the signal), and decreases with the age of the source. Because of the relatively short half-life of the β sources, the initial choice for activity necessitated having some signal pileup in order to assure an adequate source strength throughout the lifetime of the D-Zero experiment. The effect of pileup is to shift downwards the most probable (peak)value of the signal and to widen the peak in such a way as to leave the mean of the signal distribution essentially unaffected [47]. Because the most probable value of the signal is used as our measure of the response of the β cell, our effective signal tends to increase as the sources age. Fortunately, when ratios of response are examined, for instance, the ratio of response at 0.9 kV/cm to 10.9 kV/cm, the pileup effects tend to cancel. This ratio also provides excellent sensitivity to impurity concentration in the argon.

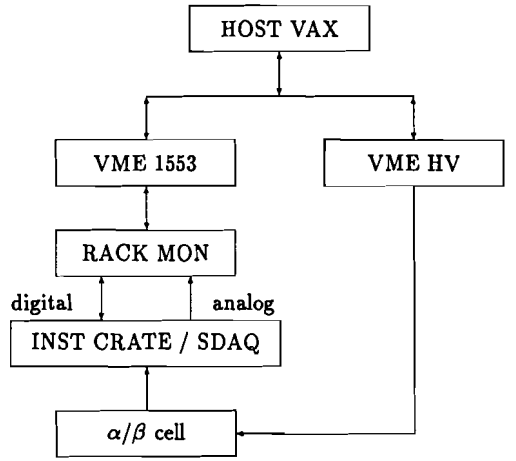

Figure A.4: System Block Diagram

A.2 Data Acquisition

Figure A.4 illustrates the interconnections between the various components of the LAr monitoring system. Each sensor is read out by a self triggered data acquisition card (SDAQ), containing amplifiers, trigger circuitry, and analog sampling electronics, The SDAQs are housed in an instrumentation crate mounted directly on the D-Zero cryostats. This crate communicates with the D-Zero monitoring system through a general purpose I/O module, the D-Zero Rack Monitor [48]. VME-based microprocessors control the rack monitors. The VME crates are, in turn, interrogated and controlled by a host VAX via a token ring network.

The VME crate houses five cards that make up the remote microprocessor (MVME) control system. This system stores and runs applications code that operates the LAr monitoring electronics. The system's CPU utilizes a Motorola

68000 series microprocessor. There is also a video card for interfacing to a small rack-mounted terminal, a memory card, a VME 1553 interface card, and a token ring interface card. The 1553 interface card links the applications code to the instrumentation crate via the rack monitor, which supports the MIL-STD-1553B communication protocol.

The rack monitor provides digital I/O, A/D, and D/A channels for hardware monitoring and control. It communicates with the MVME system over a single twisted-pair cable running to the 1553 interface card. Communication with the instrumentation crate is accomplished via three ribbon cables attached to an interface (INF) card that routes commands and data between the rack monitor and the instrumentation electronics.

Other VME crates that are part of the D-Zero monitoring and control hardware supply the high voltage to the test cells. These crates can also be controlled by the host VAX [49].

Excellent shielding and grounding techniques are essential for achieving accurate measurements of the small signals from the sensors. The entire signal path must be shielded to prevent electromagnetic pickup, and the grounding must avoid pickup of noise and extraneous signals associated with ground loops. Figure A.5 illustrates the configuration we use for all sensor pairs. The sensor, cables and SDAQ are all shielded within a Faraday cage. The sensor assembly is housed within a brass box. Penetrations include one hole for the coax signal cables, one for the HV leads, and several small perforations to provide flow of liquid argon through the sensor box. The signal cables are routed through a copper braid, which runs from the sensor box to the SDAQ shield box. The entire assembly is electrically isolated from the cryostat, except where the shield box is attached (grounded) to the cryostat.

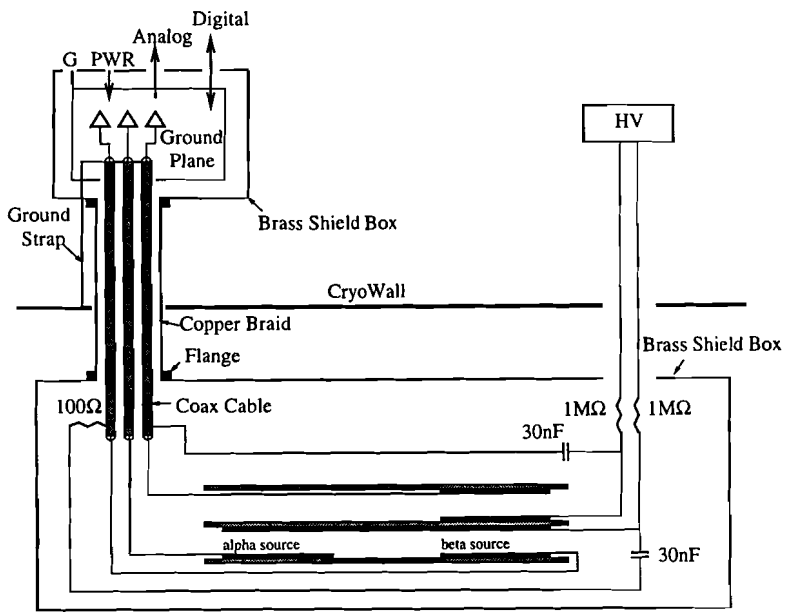

Figure A.5: Ground/Shield Configuration for Test Cells